

## Ordering phenomena in $A_{15}$ -based alloys

P. E. A. Turchi

*Lawrence Livermore National Laboratory, Condensed Matter Division (L-268), P.O. Box 808, Livermore, California 94550*

A. Finel

*Office National d'Etudes et de Recherches Aéropatiales, Division OM, Boîte Postale 72, 92322 Chatillon CEDEX, France*

(Received 26 December 1991)

From a ground-state analysis of the Ising model applied to the  $A_{15}$  crystalline structure with first-, second-, and weak third- and seventh-neighbor pair interactions, additional ordered states are predicted at the compositions  $A_5B_3$  and  $A_7B$ . Low-temperature expansions are performed and stability properties as a function of temperature and concentration are investigated by means of variational methods, within the Bragg-Williams and cluster-variation-method approximations. The results are compared with those from Monte Carlo simulations. Typical prototype  $A_{15}$ -based order-disorder phase diagrams and short-range-order diffuse-intensity calculations are presented and discussed in relation to experiment.

### I. INTRODUCTION

It has been ascertained, in the recent past, that the superconducting transition temperature, among other physical characteristics of condensed matter, was sensitive to disorder in conventional superconductors.<sup>1,2</sup> Disorder effects can result mainly from three different sources: compositional and configurational effects,<sup>3,4</sup> and also extended defect or vacancy-induced disorder.<sup>5</sup> In the present study, we will mostly concentrate on the first two closely related effects and examine in the framework of the three-dimensional Ising model the ground-state properties, i.e., at zero temperature, as well as phase stability as a function of temperature and concentration (or chemical potential) of  $A_{15}$ -based alloys. We leave for future investigations the case of ternary systems  $A_xB_yV_z$ , where the existence of vacancies  $V$  in the alloy matrix is the result of radiation damage or rapid quenching from high temperature.

Ordering processes have long been recognized to be of primary importance for describing properly crystal chemistry as well as relative phase stability and physical properties of substitutional alloys. With this regard, most of the work done so far has concentrated on alloys based upon simple crystalline structure such as fcc or bcc,<sup>6-8</sup> and very little has been investigated on complex alloys. The main reason can be attributed to the fact that simple alloys show a large variety of chemically ordered states, very often stable in a broad range of concentration, whereas most of the complex alloys exhibit a high degree of configurational order and are usually known as compounds. In the latter case, this observation leads to a straight assimilation of the crystalline structure (or bare skeleton) with the ordered configuration of the alloy (or bare skeleton plus site occupancy). This situation is often indicative of a major size effect as is the case for the Laves phases and other Frank-Kasper phases,<sup>9,10</sup> and elastic strain is a major component of their formation and stability. Meanwhile, in a few cases, it is suspected that the geometrical factors are not dominant, and the broad

range of stability with respect to concentration leads to the concept of substitutional solid solution or "electron phase."<sup>9,11</sup> Such alloys are subjected to Vegard's law, like the solid solutions of their constituents, and the Goldschmidt-Hume Rothery rule, which make their formation electronically driven.<sup>9-11</sup> Such is the case for  $A_{15}$ - (of  $Cr_3Si$  type)<sup>12</sup> and  $\sigma$ - (or  $D8_b$  of  $FeCr$  type)<sup>13</sup> based alloys. For this subset of complex alloys, it seems therefore of particular interest to investigate ordering processes which may take place as a function of temperature and concentration. In addition, after the recent discovery of a quasiperiodic icosahedral phase in  $Al_6Mn$ ,<sup>14</sup> a connection with Frank-Kasper phases was strongly supported<sup>15</sup> and, therefore, the question of how the ordering mechanism and geometrical icosahedral frustration can assist the formation of quasiperiodic phases is of major interest. Because the  $A_{15}$  structure can be considered as the simplest complex structure where local icosahedral order exists, an examination of its phase formation from a thermodynamical viewpoint can be considered as a first step towards a better understanding of these more complex phases.

In this general context, we present a detailed study of the possible existence of various ordered states for binary alloys  $A_cB_{1-c}$  possessing the  $A_{15}$  crystalline structure that we briefly recall in the following. Its space group is  $O_h^3$  (or  $Pm\bar{3}n$ ) and the primitive unit cell shown in Fig. 1(a) contains eight sites. With the origin fixed at the center  $m\bar{3}$ , six sites occupy the positions (c) with point symmetry  $D_{2d}$  (or  $\bar{4}2m$ ) and coordinates  $\frac{1}{4}(0, \pm 1, 2)$ ,  $\frac{1}{4}(\pm 1, 2, 0)$ , and  $\frac{1}{4}(2, 0, \pm 1)$ , in units of  $a$ , the lattice parameter of the  $A_{15}$  structure. These sites belong to three orthogonal sets of linear chains parallel to the three directions of the cubic cell, denoted sublattice I. The other two sites, in position (a) with point symmetry  $T_h$  (or  $m\bar{3}$ ), located at  $(0,0,0)$  and  $\frac{1}{2}(1,1,1)$  build up a body-centered-cubic structure hereafter named sublattice II. Table I gives a list of the distribution of neighbors associated with the nearest shells, for future references. Note from Figs. 1(a) and 1(b) that the  $A_{15}$  structure can be de-

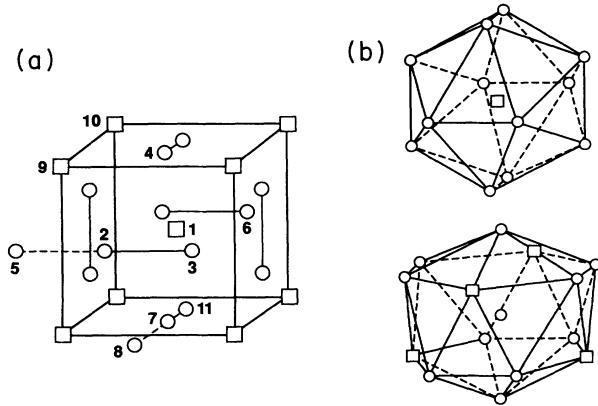


FIG. 1. (a) Primitive unit cell of the A15 crystalline structure. The circles and squares refer to sites of the set of chains and the bcc which form sublattices I and II, respectively. (b) Coordination polyhedra centered around the two inequivalent sites of A15.

scribed either as a periodic tiling of the three-dimensional Euclidean space with three irregular tetrahedra or as the interpenetration of irregular icosahedra and CN14 polyhedra.<sup>16,17</sup> Of the 70 or so compiled A15-based alloys, about 30 are transition-metal alloys and we list in Table II the less ambiguously reported systems with their homogeneity range of stability, extracted mostly from Refs. 9 and 18.

In a recent paper,<sup>19</sup> we assumed that the stability of a stoichiometric  $A_3B$  A15 transition-metal alloy (TMA) was primarily related to its electronic structure and more precisely, to the structure of its  $d$  bands. Within this basic assumption and an appropriate tight-binding description of its electronic structure, we have shown that the ordering energy,  $\Delta E(\{p_n\})$  of an A15 TMA, i.e., the energy difference between the totally ordered and disordered configurations, could be well described, in the context of the generalized perturbation method<sup>20</sup> (GPM) by the following expression:

$$\Delta E(\{p_n\}) = \frac{1}{N} \sum_n h_n (p_n - c) + \frac{1}{2N} \sum_{\substack{nm \\ n \neq m}} V_{nm} (p_n - c)(p_m - c) + \dots, \quad (1)$$

TABLE I. Number of atoms  $n_s$  and their type, at distance  $d_s$  (in units of the lattice parameter of the A15 structure) in A15 crystalline structure. A and B refer to sites belonging to sublattices I and II (see text), respectively. The last line indicates the pair types by numbers, located in Fig. 1(a).

$s$	1	2	3	4	5	6	7	8	9	10	11	12	13	14
$d_s$	0.500	0.559	0.612	0.866	0.901	0.935	1.000	1.118	1.145	1.173	1.346	1.369	1.414	1.500
Site A origin	2A	4B	8A		4B	16A	6A	8A	8B	8A	12B	16A	12A	10A
Site B origin		12A		8B	12A		6B		24A		36A		12B	
Pair type	2,3	1,2	3,4	1,9	1,5	4,5	3,5	3,6						9,10

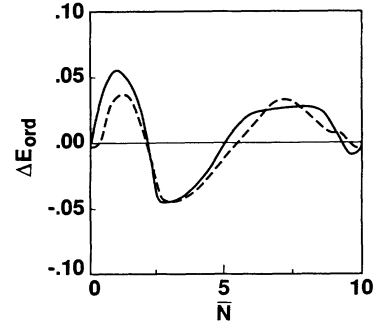


FIG. 2. Ordering energy (in canonical units, see text) as a function of  $\bar{N}$ , the average number of  $d$  electrons, for an  $A_3B$  A15-based transition metal alloy: full band calculation (solid curve) and GPM (dashed curve) results, from Ref. 19.

where  $N$  is the total number of sites, the  $p_n$  are the occupation numbers ( $p_n = 1$  or  $0$  depending on whether or not site  $n$  is occupied by an  $A$  species),  $h_n$  refers to an on-site energy (specific of any complex structure defined by a set of geometrically inequivalent sites as well as for surfaces,<sup>21</sup> and  $V_{nm}$  represents an effective pair interaction between sites  $n$  and  $m$ , given by  $V_{nm} = V_{nm}^{AA} + V_{nm}^{BB} - 2V_{nm}^{AB}$ . These interactions depend on the distance between sites  $n$  and  $m$ , and also on the alloy parameters, i.e., the number of valence electrons of both alloy components and the concentration.

This expansion (1) of the configurational contribution to the internal energy is obtained in the GPM context by a proper perturbation treatment about a state of complete disorder to take into account fluctuations of local concentration. In Fig. 2, we recall the results of a comparison between a full band calculation and the GPM expression (1) of the ordering energy as a function of the average number of  $d$ -valence electrons, in the context of the tight-binding-coherent potential approximation description of the electronic structure of the random alloy.<sup>19</sup> Note that the canonical units used to express the ordering energy displayed in Fig. 2 are of the order of 0.37 eV, as discussed in Ref. 19. The agreement is rather satisfactory and quite similar to that obtained in previously reported studies for alloys based on fcc and bcc crystalline structures.<sup>22,23</sup> In addition, expansion (1) is, in most cases, rapidly convergent, and usually multisite interac-

TABLE II. Compilation of *A15*-based alloys (after Refs. 9 and 17). The homogeneity range (indicated in parentheses) is given in atomic percent of the majority element listed as the first element.

TiHg(75)	VGa(69–82)	NbAl(68–82)	TaRh(72–78)	MoAl(72–78)
TiTi(80)	VSi(74–81)	NbGa(75)	TaPt(84–87)	MoGa(75)
TiSb(75)	VGe(76)	NbIn(75)	TaAu(82–85)	MoSi(75)
TiIr(73–75)	VSn(79–80)	NbSi(81.2)	CrGa(77)	MoGe(75)
TiPd(80)	VOs(52)	NbGe(80–82)	CrSi(74–78)	MoSn(75)
TiPt(72–77)	VCo(75)	NbSn(74–82)	CrGe(75–80)	MoTe(54)
TiAu(75)	VRh(63–74)	NbSb(73–76)	CrRu(75)	MoOs(74–77)
ZrTi(80)	VIr(61–76)	NbOs(71–75)	CrOs(75)	MoIr(74–79)
ZrSn(80)	VNi(77–79)	NbRh(75)	CrRh(77–78)	MoPt(82)
ZrAu(75)	VPd(74–76)	NbIr(71–79)	CrIr(73–82)	
	VPt(67–81)	NbPt(74–79)		
	VAu(78–81)	NbAu(72–83)		

tions are negligible compared with pair interactions.

One should note that the GPM provides a proper connection between electronic structure calculations and thermodynamical properties, and above all, a formal justification of the validity of the three-dimensional generalized Ising model when dealing with ordering processes in substitutional alloys. Such a model was used successfully to search for the most probable ground states (i.e., at  $T=0$  K) as a function of the magnitude of the pair (and eventually multisite) interactions which build up the ordering energy.<sup>24</sup> Finally, at  $T\neq 0$  K, this Ising model allows the calculation of equilibrium thermodynamical properties when combined with a variational method such as the cluster-variation-method approximation,<sup>25,26</sup> or with Monte Carlo simulations.<sup>27,28</sup> We will see that such ordering theory applied to nonsymmorphic complex structures, i.e., to lattices characterized by several crystallographically nonequivalent sites, as is the case for *A15*, produces a number of peculiarities.

Thus, the study of ordering processes in *A15*-based alloys will be performed by using the following Hamiltonian:

$$H = \sum_{\langle nm \rangle} J_{nm} \sigma_n \sigma_m - h \sum_n \sigma_n, \quad (2)$$

where  $\sigma_n$  is a spinlike variable related to  $p_n$  by  $\sigma_n = 2p_n - 1$ ,  $h$  is the chemical potential, and  $J_{nm} = V_{nm}/4$ . The first sum runs over the pair  $nm$  of sites. Any configuration of an alloy, at  $T=0$  K, is specified by the set  $\{\sigma_n\}$ .

Rigorously, because of the existence of two inequivalent sites [denoted (a) and (c)] in the *A15* structure, the last term on the right-hand side (rhs) of expression (2) should be rewritten as  $\sum_{\alpha} h_{\alpha} \sum_n \sigma_{n_{\alpha}}$ , where  $\alpha$  refers to sublattices I and II. These single-site terms  $h_{\alpha}$  cannot be ignored for an accurate determination of stability energies although their contribution was shown to be small.<sup>19</sup> Furthermore, as apparent in expression (2), they will have little influence on order-disorder phenomena taking place in *A15*-based alloys, phenomena dominantly accounted for by the first term of the rhs of expression (2).

For these reasons, we will omit in what follows this extra complication. Moreover, we will assume that the

effective pair interactions  $J_{nm}$  in (2) are concentration independent, for simplicity and without altering the conclusions of the present study.

The rest of the paper is organized as follows. In Sec. II, we present the ground-state analysis of the Ising model applied to the *A15* structure with first-, second- and weak third- and seventh-neighbor pair interactions. In Sec. III, we perform low-temperature expansions and give an accurate description, in both the canonical and grand-canonical ensembles, of phase stability properties at low temperature. In Sec. IV, we discuss these properties at any temperature and concentration (or chemical potential) by using a variational method, namely the cluster variation method, for various regimes of pair interactions. The results will be compared with those obtained in the Bragg-Williams approximation and by the Monte Carlo method. Finally, in Sec. V, the resulting prototype *A15*-based order-disorder phase diagrams are discussed in relation to calculated short-range-order diffuse-scattering-intensity maps and experiment, before adding some concluding remarks on the electronic structure properties of the most promising *A15*-based ground states.

## II. GROUND-STATE ANALYSIS

In the following analysis, we will consider successive groups of pair interactions, in agreement with the hierarchy deduced from electronic structure calculations,<sup>19</sup> that is,  $|J_1|, |J_2| > |J_3| \gg |J_{s \geq 4}|$ . Note that, from now on,  $J_s$  refers to a pair interaction between a site located at the origin and the other in the  $s$ th-neighbor shell.

### A. $\{J_1, J_2\}$ ground-state analysis

The first- and second-neighbor pair interactions,  $J_1$  and  $J_2$ , which are considered here, couple, for example, sites 2 and 3, and 1 and 2 in Fig. 1(a), respectively. The simplest cluster yielding the configurational polyhedron<sup>24,29–31</sup> is the isosceles triangle which connects a site of sublattice II to two neighboring sites of sublattice I [see triangle  $\{1,2,3\}$  of Fig. 1(a)]. This polyhedron has six vertices associated with the six possible configurations on a triangle. After the symmetry  $A \leftrightarrow B$  is taken into ac-

TABLE III. Summary of the ground-state analysis within the isosceles triangle polyhedron of configuration.  $x_i$  ( $\mu_i$ ) refers to a correlation function (degeneracy or multiplicity) associated with an  $i$ -point cluster. Full or empty circles (sites of sublattice I) and squares (sites of sublattice II) refer to  $A$  or  $B$  species.

Correlation Function Configuration	$x_1$	$x'_1$	$x_2$	$x'_2$	$x_3$	Energy	Ordered State and Composition
	1	1	1	1	1	$-8h + 6J_1 + 24J_2$	F (A)
	1	-1	1	-1	-1	$-4h + 6J_1 - 24J_2$	A15 ( $A_3B$ )
	0	1	-1	0	-1	$-2h - J_1$	X ( $A_5B_3$ )
Degeneracy $\mu_i$	6	2	6	24	12		

count, we are left with three vertices, as defined in Table III [if one assumes that the on-site terms of (2) are the same, and equal to  $h$ , for both inequivalent sites]. The configurations attached to each vertex are constructive and correspond to: pure metal  $A$ ,  $A_3B$  (the so-called A15 configuration, of  $\text{Cr}_3\text{Si}$  type), and  $A_5B_3$ , named hereafter  $F$ , A15, and  $X$ , respectively. The new configuration  $X$  is described by sublattice II fully occupied by  $A$  species and alternation of  $A$  and  $B$  species along each individual chain of sublattice I (see Fig. 3). The order along each chain corresponds to the magnetic analog of the antiferromagnetic order. At this point, no coupling between the chains exists, but it is anticipated, for configurational entropy reason, that the most symmetrical configuration will remain at  $T \neq 0$  K. The zero-temperature phase diagram in the  $(K_1, K_2)$  representation, where  $K_1 = 6J_1/h$  and  $K_2 = 24J_2/h$ , and the resulting ordering map in  $(J_1, J_2)$  are given in Figs. 4(a) and 4(b), respectively. Each sector in Fig. 4(b) is associated with a sequence of ordered structures when the concentration in  $B$  species increases. For intermediate concentration, the ground state is given by an appropriate mixture of the neighboring ordered configurations. From this simple analysis, we conclude that the three

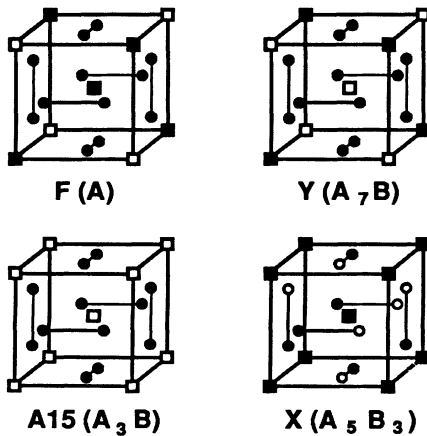


FIG. 3. Ground states based on the A15 crystalline structure. Each configuration is referred to by its name and its composition (in parentheses).

configurations  $F$ , A15, and  $X$  may exist provided  $\frac{1}{4} \leq \alpha_2 = J_2/J_1 \leq \frac{1}{2}$ .

A natural step towards a better understanding of phase stability at finite temperature and before performing low-temperature expansions, whenever it is possible, is to study the degeneracy ( $d$ ) and the residual entropy ( $S$ ) of each configuration. Obviously  $F$  and A15 are nondegenerate phases, i.e.,  $d = 1$  with zero residual entropy. In the case of the  $X$  phase, if  $L$  is the size of the lattice (in units of the lattice parameter) along the three directions of the cubic unit cell, the number of chains is  $3L^2$  and the only constraint is the antiferromagnetic order along the chains, therefore

$$d = 2^{3L^2} \quad \text{and} \quad S = \frac{1}{8L^3} \ln d,$$

that is,  $d = \infty$  and  $S = 0$  in the thermodynamic limit.

For the phase equilibria, let us first examine the case  $F$ -A15. The two allowed configurations of the isosceles triangle leave the  $2L^3$  sites of sublattice II free of constraint, hence:

$$d = 2^{2L^3} \quad \text{and} \quad S = \frac{1}{8L^3} \ln 2^{2L^3} = \frac{1}{4} \ln 2,$$

which gives, in the thermodynamic limit,  $d = \infty$  and  $S = \frac{1}{4} \ln 2$ . In the case A15- $X$ , the constraint imposed by the coexistence of the two configurations of the isosceles triangle leads to  $d = d_X$  infinite and  $S = 0$ . Finally for the  $F$ - $X$  equilibrium, the sites of infinite sublattice II are pure  $A$ , whereas a choice exists for the chains: each first-neighbor pair along a chain may be either pure  $A$  or  $AB$ .

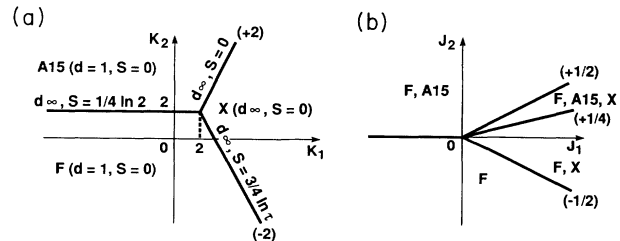


FIG. 4. (a) Ground-state phase diagram in  $(K_1, K_2)$ , where  $K_1 = 6J_1/h$  and  $K_2 = 24J_2/h$ , with degeneracy  $d$  and residual entropy  $S$  for each configuration and phase equilibrium. (b) Ordering map in  $(J_1, J_2)$ .

Therefore  $d = \infty$  and  $S = \frac{3}{4} \ln \tau$ , where  $\tau$  is the golden number  $\tau = (1 + \sqrt{5})/2$ , as shown in Appendix A.

These results, reported in Fig. 4(a), show that the only possible low-temperature expansion which can be performed concerns the  $A15$ - $X$  phase equilibrium.<sup>24</sup> In the next section, we will examine the effect of introducing a third-neighbor pair interaction,  $J_3$ , which connects two sites belonging to two orthogonal chains, such as the pair  $\{2, 4\}$  in Fig. 1(a).

### B. $\{J_1, J_2, J_3\}$ ground-state analysis

For physical reasons, we restrict our study to the case  $|J_3| \ll |J_1|, |J_2|$ . Then, the following questions can be answered exactly: (i) Does  $J_3$  stabilize other ground states than the ones previously obtained? (ii) How does  $J_3$  modify the previous equilibria? In order for the phase diagram in  $(J_1, J_2)$  to change discontinuously with the introduction of  $J_3$ , which would, in that case, give rise to an additional ordered state, this state must already exist, being degenerate with one of the three configurations  $F$ ,  $A15$ ,  $X$  of the  $\{J_1, J_2\}$  analysis. Therefore, each sector of the phase diagram in  $(J_1, J_2)$  should be reviewed, and two cases should be examined: Either the sector corresponds to a nondegenerate situation, which implies it should transform continuously with  $J_3$ , i.e., an additional ordered state cannot appear in a single-phase domain, or the sector corresponds to a degenerate situation, and in that case,  $J_3$  can favor one of the degenerate ground state of the  $\{J_1, J_2\}$  analysis. The degeneracy will be removed if the ground states do not have the same correlation function associated with the third-neighbor pair,  $y_3$ .

It is clear that the only possible ground state which can be *a priori* destabilized by the introduction of  $J_3$  is the  $X$  phase. It is also obvious that all phases possessing the  $X$  type of order have the same  $y_3, y_3 = 0$ . Hence, the degeneracy of  $X$  is unchanged with  $J_3$ , i.e.,  $d = \infty$  and  $S = 0$ , because any translation of each individual antiferromagnetically ordered linear chain does not cost any additional energy.

To conclude this section, we need to examine the three equilibria. For  $F$ - $A15$ ,  $d$  is infinite but only concerns sublattice II, therefore  $y_3$  is the same for all the degenerate states. Moreover, because  $F$  and  $A15$  have the same  $y_3, y_3 = 1$ , a vertical limit exists with respect to the  $(J_1, J_2)$  plane. For  $A15$ - $X$  and  $F$ - $X$ , because  $X$  is not affected by  $J_3$  ( $y_3 = 0$ ), no extra domain exists but the limits  $F$ - $X$  and  $A15$ - $X$  are not vertical ( $y_3^{A15} = y_3^F \neq y_3^X$ ).

Hence, we have shown that the introduction of the third-neighbor pair interaction  $J_3$  does not introduce any extra configuration and preserves the topology of the ordering map, as illustrated in Fig. 5, provided  $J_3$  is small compared with  $J_1$  and  $J_2$ .

From what has been studied so far, it is anticipated that the phase diagram at finite temperature will show peculiarities associated with nonzero residual entropy and infinite degeneracy (see Sec. IV). The  $F$ - $A15$  equilibrium corresponds to a so-called superdegenerate situation<sup>24,32,44</sup> and from the hard-sphere analysis presented in

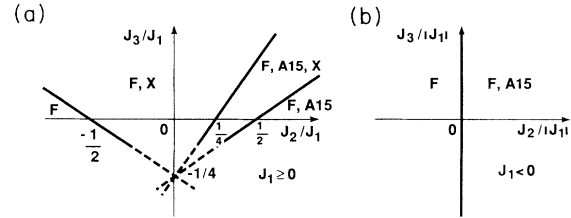


FIG. 5. Ordering map in  $(J_2/J_1, J_3/J_1)$  for (a)  $J_1 \geq 0$  and (b)  $J_1 < 0$ .

Appendix B, it is shown that no transition exists at finite angle and that a standard Bragg-Williams treatment is exact at low temperature. Moreover, if one considers the  $X$  phase at its composition  $A_5B_3$  and  $\bar{X}$  at  $A_3B_5$ , the  $X$  and  $\bar{X}$  superstructures have the same symmetry and only differ by the bcc sublattice occupancy (mainly  $A$  atoms for  $X$  and  $B$  atoms for  $\bar{X}$ ), as it is the case for  $A15$  and  $F$ . Therefore, what was said for the  $F$ - $A15$  equilibrium also applies to the  $X$ - $\bar{X}$  one. Finally, up to and including  $J_3$ , at  $T$  strictly different from 0 K, the chains of the  $X$  phase will disorder and the symmetry of the overall underlying lattice will be restored. Indeed, the low-energy excitation spectrum of the  $X$  phase is associated with a change of order  $A \leftrightarrow B$  along any semi-infinite linear chain. In other words, a phase diagram at nonzero temperature will not exhibit the long-range order (LRO) of  $X$  type (except at  $T$  strictly equal to 0 K). Thus, in order to stabilize the  $X$  phase at finite temperature, it is necessary to introduce longer-range interactions.

### C. $\{J_1, J_2, J_3, J_7\}$ ground-state analysis

It is easy to realize that the first pair interaction which lifts the degeneracy of the  $X$  phase and stabilizes it at finite temperature is the seventh pair interaction which connects, in particular, two parallel chains through, for example, sites 3 and 6 of Fig. 1(a), referred to as  $J_7^{(1)}$ . One should note that two other types of pair, at the same distance, exist and, in principle, should be differentiated from  $J_7^{(1)}$  for geometrical and electronic reasons [see sites 5 and 3, and 9 and 10 of Fig. 1(a)]. For the sake of simplicity, we assume that the seventh pair interaction along the chains [such as the one involving the pair 5-3 of Fig. 1(a)] is equal to the one between parallel chains, namely  $J_7^{(1)}$ , and we note  $J_7^{(2)}$  the seventh pair interaction which pertains to the bcc sublattice [e.g., the interaction between sites 9 and 10 of Fig. 1(a)].

$F$  and  $A15$  are nondegenerate phases and  $J_7$  (small in magnitude) does not destabilize them. For the  $X$  phase, the degeneracy associated with the chains of sublattice I is removed by  $J_7^{(1)}$  and, according to the sign of  $J_7$ , the chains, parallel to each cubic direction, will be in phase (superstructure  $X_1$  for  $J_7 < 0$ ) or in antiphase (superstructure  $X_2$  for  $J_7 > 0$ ), as illustrated in Fig. 6, and for both cases the degeneracy is  $d = 2^3$ . With respect to the equilibria, the infinite degeneracy of  $F$ - $A15$  is removed and sublattice II orders. For  $J_7 < 0$ , a “ferromagnetic” order on the bcc sublattice takes place and  $d = 4$ . This type of order characterizes both  $A15$  and  $F$ , and consequently

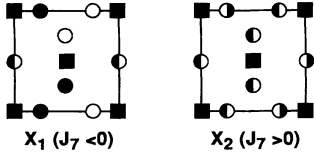


FIG. 6. Projection along the [001] direction of the ground states  $X_1$  and  $X_2$  at the composition  $A_5B_3$  ( $X_1$  corresponds to  $X$  of Fig. 3). Full and empty circles or squares refer to  $A$  and  $B$  species, respectively.

the equilibrium  $F$ - $A15$  is not perturbed. On the contrary, for  $J_7 < 0$ , an additional ground state, called  $Y$  at the composition  $A_7B$  (see Fig. 3) is stabilized, with  $d = 4$ . This state is defined by sublattice I occupied by pure species  $A$ , in addition to an “antiferromagnetic” order among sites of each simple cubic skeleton which forms sublattice II. This order on the bcc sublattice corresponds to  $B32$  of NaTl type. One should note that  $Y$  simply results from the approximative treatment which only includes the second pair interaction of the bcc lattice,  $J_7^{(2)}$ . More generally, the interactions of the  $A15$  structure which only couple sites of sublattice II would give the known ground state of the bcc lattice.<sup>24,30</sup> Similarly, the interactions connecting sites of individual chains would generate the ground states of the linear chain<sup>24,33</sup> (see Table IV for a list of correspondence). The energies of the ground states, per unit cell, are given by

$$\begin{aligned} E_F &= -8h + 6J_1 + 24J_2 + 24J_3 + 18J_7^{(1)} + 6J_7^{(2)}, \\ E_Y &= -6h + 6J_1 + 24J_3 + 18J_7^{(1)} - 6J_7^{(2)}, \\ E_{A15} &= -4h + 6J_1 - 24J_2 + 24J_3 + 18J_7^{(1)} + 6J_7^{(2)}, \\ E_{X_1} &= -2h - 6J_1 + 18J_7^{(1)} + 6J_7^{(2)}, \\ E_{X_2} &= -2h - 6J_1 - 6J_7^{(1)} + 6J_7^{(2)}. \end{aligned} \quad (3)$$

Neglecting  $J_3$  and setting up  $J_7^{(1)} = J_7^{(2)} = J_7$  in the following analysis, for representation purposes, we obtain, near  $h = h_c^{(1)} = 12J_2$ , the ground-state diagram of Fig. 7(a) for the  $F$ - $A15$  equilibrium. For  $A15$ - $X$ , the degeneracy inherited from the  $X$  phase is removed and  $d = 8$ . The resulting ground-state phase diagram is displayed in Fig. 7(b) near  $h = h_c^{(2)} = 6J_1 - 12J_2$ . Finally, for  $F$ - $X$ , because of the two possible configurations of the isosceles triangle (sites 1, 2, and 3 of Fig. 1(a)) and the additional constraint

TABLE IV. Correspondence between neighbor shells as described on an  $A15$  crystalline structure and on the linear chain or the bcc lattice.

	1	7	14	26	
$A15$	1	7	14	26	
Linear chain	1	2	3	4	
<hr/>					
$A15$	4	7	13	17	20
bcc	1	2	3	4	5

that for  $J_7 < 0$  ( $J_7 > 0$ ), the linear chains couple “(anti)ferromagnetically,” it is easily seen that the degeneracy of each set of parallel chains is  $d = \tau^{2L}$ . In other words, a configuration along an individual chain imposes the configuration of all parallel chains. Hence, as the three sets of parallel chains, building up sublattice I, are independent (with  $J_3 = 0$ ), the total degeneracy is  $d = (\tau^{2L})^3$ , and  $S = 0$ . The ground-state diagram is given in Fig. 7(c) around  $h = h_c^{(3)} = 6J_1 - 12J_2$ .

From now on, we will assume the following hierarchy:  $J_1, J_2 \gg J_3, J_7$  and  $J_7 < 0$ , which can be justified on physical ground from electronic structure calculations.<sup>19,22</sup> Because a small  $J_3$  does not generate any additional ground state or change the topology of the ordering maps, this interaction will be ignored and the only purpose of retaining  $J_7$  (especially  $J_7^{(1)}$ ) is twofold: first to stabilize the  $X$  phase at finite temperature, and second, to allow low-temperature expansions to be performed.

### III. LOW-TEMPERATURE EXPANSIONS

With the previous assumptions, the three phases  $F$ ,  $A15$ ,  $X$  can be stable at finite temperature for  $\alpha_2 = J_2/J_1$  such that  $\frac{1}{4} \leq \alpha_2 \leq \frac{1}{2}$  [see Fig. 4(b)]. Moreover because at  $T = 0$  K, the degeneracies and residual entropies of the three most important equilibria are  $d = 8$ ,  $S = 0$  for  $X$ - $A15$ ,  $d = 4$ ,  $S = 0$  for  $F$ - $A15$ , and  $d = 16$ ,  $S = 0$  for  $X$ - $\bar{X}$ , low-temperature expansions can be performed.<sup>24</sup> These series expansions are based on the intuitive idea that the equilibrium state of a system, at sufficiently low temperature, corresponds to a small perturbation of its ground state. It is obvious that such will be the case for a nondegenerate ground state, and low-temperature expansion is estimated by taking successively into account excitation energies in increasing order from the ground-state energy. The problem is more complex when dealing with de-

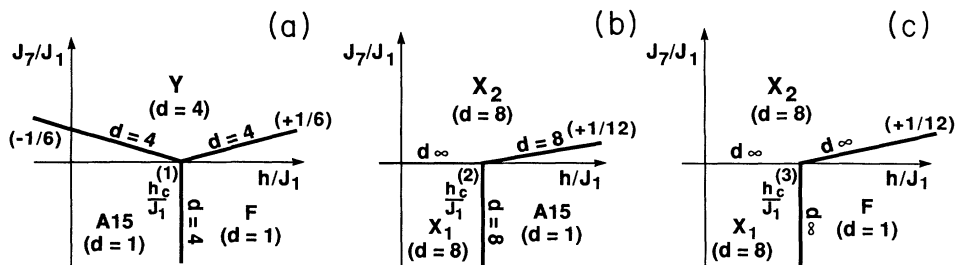


FIG. 7. Ground-state phase diagram in  $(h/J_1, J_7/J_1)$  around (a)  $h_c^{(1)} = 12J_2$ , (b)  $h_c^{(2)} = 6J_1 - 12J_2$ , and (c)  $h_c^{(3)} = h_c^{(2)}$ .  $d$  refers to the degeneracy.

generate ground states, especially when  $d$  is infinite. The theory of Pirogov and Sinai,<sup>34</sup> which deals with finite degeneracy, was extended to infinite degeneracy and zero residual entropy, provided that the energy of an excitation increases with the number of occupied sites, the so-called regularity condition.<sup>24,35</sup> Such calculations allow an accurate determination, at low temperature, of the zone boundaries between the existing phases, in both the canonical (temperature versus concentration) and grand-canonical (temperature versus chemical potential) ensembles. We will first consider the  $A15$ - $X$  (implicitly  $X_1$ , because  $J_7 < 0$ ) phase equilibrium, the only case which can be studied within the first and second pair interaction analysis, before considering the three most important phase equilibria in the  $J_1, J_2$ , and  $J_7$  ( $J_7 < 0$ ) analysis.

#### A. Low-temperature expansion with $J_1$ and $J_2$

Let us call  $\Delta E_{\alpha}^i$ , the excitation energy per unit cell of superstructure  $\alpha$  relative to site  $i$ ,  $i$  being located by a number as in Fig. 1(a) and occupied, in the ground-state configuration  $\alpha$ , as in Fig. 3. For  $A15$  and  $X$ , we obtain the following set of equations, where  $\mu_{\alpha}^i$  indicates the multiplicity of site  $i$  for the ground state  $\alpha$ :

$$\begin{aligned} \Delta E_{A15}^1 &= -2h + 24J_2, & \mu_{A15}^1 &= 2, \\ \Delta E_{A15}^2 &= 2h - 4J_1 + 8J_2, & \mu_{A15}^2 &= 6, \\ \Delta E_X^1 &= 2h, & \mu_X^1 &= 2, \\ \Delta E_X^2 &= 2h + 4J_1 - 8J_2, & \mu_X^2 &= 3, \\ \Delta E_X^3 &= -2h + 4J_1 + 8J_2, & \mu_X^3 &= 3. \end{aligned} \quad (4)$$

From (3), the  $A15$ - $X$  equilibrium is realized for  $h_c/J_1 = 6 - 12\alpha_2$  and  $\frac{1}{4} \leq \alpha_2 \leq \frac{1}{2}$  (see, also, Sec. II A). At this particular value of the chemical potential, the excitation energies (4) vary with  $\alpha_2$  ( $=J_2/J_1$ ) as indicated in Fig. 8. One should mention that an additional energy relative to the  $X$  phase has to be considered. It corresponds to the excitation, from the ground-state configuration, of a chain of the  $X$  phase to a configuration where the occu-

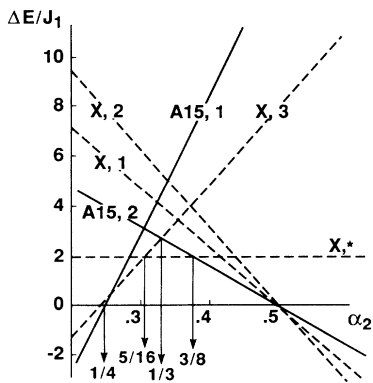


FIG. 8. Excitation energies (per unit cell) of the  $A15$  and  $X$  superstructures, at  $h_c/J_1 = 6 - 12\alpha_2$ , as a function of  $\alpha_2$ . Each line is associated with a configuration and a site number or  $a^*$  for the half-chain excitation (see text).

pancy of half the chain has been flipped; this energy is equal to  $\Delta E_X^* = 2J_1$ , with  $\mu_X^* = 12$ . From Fig. 8, the lowest-excitation-energy spectrum implies that for  $\frac{1}{4} \leq \alpha_2 \leq \frac{3}{8}$ ,  $X$  becomes more stable than  $A15$  at low temperature, whereas the contrary is true for  $\frac{3}{8} \leq \alpha_2 \leq \frac{1}{2}$ . As was discussed in Sec. II B, the  $X$  phase disorders at  $T$  strictly different from 0 K, in this simple analysis in  $\{J_1, J_2\}$ . Therefore, one should refer to the  $X$  phase more appropriately as an  $A15$  phase with the short-range order of  $X$  type, as it will be demonstrated in Sec. IV B. We will call this configuration  $A15'$ . The grand-canonical results are schematically illustrated in Figs. 9(a) and 9(b). If  $\Delta E^{\alpha-\beta}$  is the energy difference between the two superstructures  $\alpha$  and  $\beta$ , and  $\Delta h = h - h_c$ , then  $\Delta E^{A15'-X} = -2\Delta h$  and the equations which describe the phase boundaries follow. Thus, we define the three regimes:

$$\begin{aligned} \frac{1}{4} \leq \alpha_2 \leq \frac{5}{16}: & \quad -\Delta E = kT\mu_X^3 e^{-\beta\Delta E_X^3} \\ & \quad \text{or } \Delta h \sim \frac{3}{2}kTe^{-\beta(-8+32\alpha_2)}, \\ \frac{5}{16} \leq \alpha_2 \leq \frac{3}{8}: & \quad -\Delta E = kT\mu_X^* e^{-\beta\Delta E_X^*} \text{ or } \Delta h \sim 6kTe^{-2\beta}, \\ \frac{3}{8} \leq \alpha_2 \leq \frac{1}{2}: & \quad -\Delta E = kT\mu_{A15}^2 e^{-\beta\Delta E_{A15}^2} \\ & \quad \text{or } \Delta h \sim -3kTe^{-\beta(8-16\alpha_2)}, \end{aligned} \quad (5)$$

where  $\beta = J_1/kT$ , and  $k$  is the Boltzmann's constant.

In order to define similar equations in the canonical representation, one has to evaluate the concentration  $c$  of the alloy  $A_cB_{1-c}$  as a function of  $T$  and  $h$ , according to

$$2c - 1 = \frac{1}{8} \frac{\partial F}{\partial h},$$

where the factor 8 is the total point degeneracy in the unit cell and  $F$  is the free energy per unit cell. For a

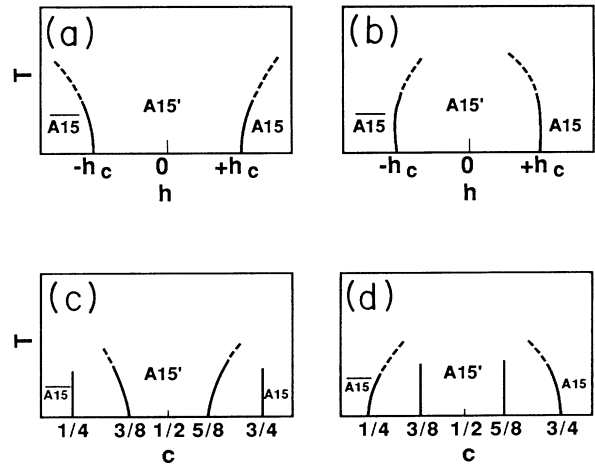


FIG. 9. Schematic representation of phase diagrams in the grand-canonical [(a) and (b)] and in the canonical [(c) and (d)] ensembles, for the two regimes of interactions:  $\frac{1}{4} \leq \alpha_2 \leq \frac{3}{8}$  [(a) and (c)], and  $\frac{3}{8} \leq \alpha_2 \leq \frac{1}{2}$  [(b) and (d)].

given superstructure  $\alpha$  and values of  $T$  and  $h$ ,  $F$  takes the form

$$F_\alpha = E_\alpha - \mu_\alpha^i k T e^{-\beta \Delta E_\alpha^i(h, J_1, J_2)}$$

Along the phase boundary and in the first-order approximation of the low-temperature expansion, the concentration associated with the highest  $\Delta E$  is constant as a function of temperature, whereas the concentration of the superstructure possessing the lowest excitation energy varies as  $e^{-\beta \Delta E}$  (if  $\Delta E$  varies with  $h$ ). Hence,

$$\begin{aligned} \frac{1}{4} \leq \alpha_2 \leq \frac{5}{16}: c_{A15} \sim \frac{3}{4} \\ \text{and } c_X \sim [5 + 3e^{-\beta(-8+32\alpha_2)}] / 8, \\ \frac{5}{16} \leq \alpha_2 \leq \frac{3}{8}: c_{A15} \sim \frac{3}{4} \text{ and } c_X \sim \frac{5}{8}, \\ \frac{3}{8} \leq \alpha_2 \leq \frac{1}{2}: c_{A15} \sim 3[1 - e^{-\beta(8-16\alpha_2)}] / 4 \\ \text{and } c_X \sim \frac{5}{8}, \end{aligned} \quad (6)$$

as illustrated in Figs. 9(c) and 9(d).

Regarding the other equilibria,  $\bar{F}(B)$ - $\overline{A15}(AB_3)$ ,  $\bar{X}(A_3B_5)$ - $X(A_3B_3)$ , and  $A15(A_3B)$ - $F(A)$ , their respective two phase boundaries, if they exist, should not reach their standard limits  $c=0$  and  $\frac{1}{4}$ ,  $c=\frac{3}{8}$  and  $\frac{5}{8}$ , and  $c=\frac{3}{4}$  and 1, respectively, due to the nonzero value of their residual entropy  $S = \frac{1}{2} \ln 2$  (see Sec. II A). In fact, the hard-sphere treatment presented in Appendix B shows that no transition line exists at finite angle, i.e., for any value of  $h$ . Therefore these phase boundaries simply do not show up in this  $\{J_1, J_2\}$  analysis.

#### B. Low-temperature expansion with $J_1, J_2 > 0$ and $J_7 < 0$

With the introduction of  $J_7$ , the half-chain excitation of the  $X$  phase is no longer allowed and therefore we have the following results for the  $A15(A_3B)$ - $X$  (or  $X_1$  at  $A_5B_3$ ) equilibrium:

$$\begin{aligned} \frac{1}{4} \leq \alpha_2 \leq \frac{1}{3}: \Delta h \sim \frac{3}{2} k T e^{-\beta(-8+32\alpha_2-12\alpha_7)}, \\ c_{A15} \sim \frac{3}{4}, \\ c_X \sim [5 + 3e^{-\beta(-8+32\alpha_2-12\alpha_7)}] / 8, \\ \frac{1}{3} \leq \alpha_2 \leq \frac{1}{2}: \Delta h \sim 3k T e^{-\beta(8-16\alpha_2-12\alpha_7)}, \\ c_{A15} \sim 3[1 - e^{-\beta(8-16\alpha_2-12\alpha_7)}] / 4, \\ c_X \sim \frac{5}{8}, \end{aligned} \quad (7)$$

where  $\Delta h = h - h_c$  and  $h_c/J_1 = 6 - 12\alpha_2$ , and  $\alpha_7 = J_7/J_1$ .

For the  $F$ - $A15$  equilibrium, we define the lowest excitation energies per unit cell as

$$\begin{aligned} \Delta E_{A15}^1 &= -2h + 24J_2 - 12J_7, \quad \mu_{A15}^1 = 2, \\ \Delta E_{A15}^2 &= 2h - 4J_1 + 8J_2 - 12J_7, \quad \mu_{A15}^2 = 6, \\ \Delta E_F^1 &= 2h - 24J_2 - 12J_7, \quad \mu_F^1 = 2, \\ \Delta E_F^2 &= 2h - 4J_1 - 8J_2 - 12J_7, \quad \mu_F^2 = 6. \end{aligned} \quad (8)$$

At equilibrium,  $h_c = 12J_2$ , and the resulting excitation en-

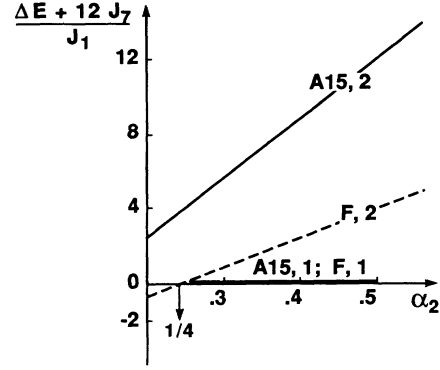


FIG. 10. Same as in Fig. 8 for the  $A15$  and  $F$  configurations, at  $h_c = 12J_2$ .

ergy spectrum, given in Fig. 10, shows that  $F$  is more stable than  $A15$  for any value of  $\alpha_2$  in the range  $[\frac{1}{4}, \frac{1}{2}]$ , and the phase boundaries are given by

$$\begin{aligned} \Delta h &\sim -\frac{3}{2} k T e^{-\beta(-4+16\alpha_2-12\alpha_7)}, \\ c_F &\sim 1 - \frac{3}{4} e^{-\beta(-4+16\alpha_2-12\alpha_7)}, \\ c_{A15} &\sim \frac{3}{4}, \end{aligned} \quad (9)$$

where  $\Delta h = h - h_c$  and  $h_c/J_1 = 12\alpha_2$ .

Finally, for the  $X(A_5B_3)$ - $\bar{X}(A_3B_5)$  equilibrium, we obtain

$$h \sim 0, \quad c_X \sim \frac{5}{8}, \quad c_{\bar{X}} \sim \frac{3}{8}. \quad (10)$$

The results (7), (9), and (10) are summarized in Fig. 11. One should note that the  $X(A_5B_3)$  and  $\bar{X}(A_5B_3)$  superstructures share the same group of symmetry, and therefore the  $X$ - $\bar{X}$  line corresponds to a particular transition between the two possible "ferromagnetically ordered" bcc sublattices. A similar comment applies to the  $F$ - $A15$  line.

## IV. PHASE STABILITY PROPERTIES AT FINITE TEMPERATURE

### A. Generalities

The low-temperature expansion study presented in the previous section leads to a detailed description of the rel-

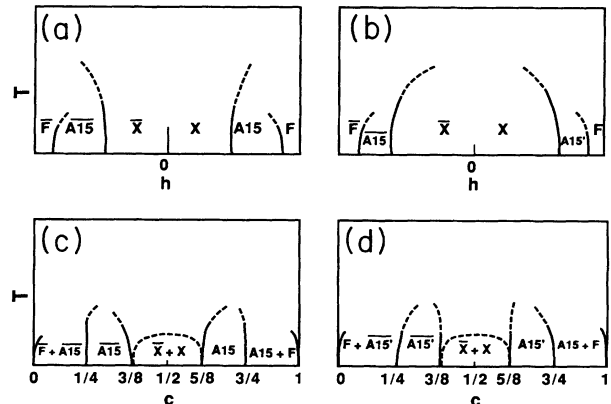


FIG. 11. Same as in Fig. 9 for the two regimes of interactions:  $\frac{1}{4} \leq \alpha_2 \leq \frac{1}{3}$  [(a) and (c)], and  $\frac{1}{3} \leq \alpha_2 \leq \frac{1}{2}$  [(b) and (d)];  $J_7 < 0$ .



atively low-temperature part of the phase diagram. In order to extend this knowledge to any temperature and concentration, the calculation of the equilibrium free energy is required. This quantity can be obtained either by a variational method such as the cluster variation method<sup>25,26</sup> (CVM), after a maximum cluster or set of maximum clusters has been selected to approximate the configurational entropy, or by performing Monte Carlo (MC) simulations.<sup>27,28</sup> Because the pair interactions which build up the ordering energy are assumed to be concentration independent, for the sake of simplicity, the calculations can be carried out either at constant concentration, i.e., in the canonical representation, or at constant chemical potential, i.e., in the grand-canonical representation, at any given temperature.

For practical reasons, let us first recall the free-energy-functional form in a way consistent with the basic CVM equations,<sup>26</sup> and discuss the possible CVM approximations which can be applied to the present *A15* case, before commenting on the characteristics of our MC scheme.

### 1. Cluster variation method

Retaining only pair interactions, the configurational part of the internal energy will be written as

$$U^\alpha(c, T) = \sum_s \sum_r \gamma_{s,r}^\alpha J_s \xi_{s,r}^\alpha(c, T), \quad (11)$$

where  $s$  is the coordination shell index and  $r$  denotes a type of pair. The latter index specifies the various inequivalent  $s$ -neighbor pairs which may exist for a particular ordered structure  $\alpha$ .  $\gamma_{s,r}^\alpha$  stands for the number per unit cell of  $s$ -neighbor pairs of type  $r$  in the superstructure  $\alpha$  (for a completely random configuration, these coefficients correspond to half the coordination numbers at their respective shell  $s$ ).

As usual, the pair correlation functions are given by

$$\xi_{s,r}^\alpha = \langle \sigma_n \sigma_{n+s} \rangle_r^\alpha, \quad (12)$$

where  $\langle \dots \rangle$  denotes a statistical ensemble average. These functions are determined by the symmetry of the superstructure  $\alpha$  and calculated by minimizing the CVM free-energy functional. This functional is constructed by adding to  $U$  the term  $-TS^\alpha$ , where the CVM configurational entropy takes the form

$$S^\alpha = -k \sum_{m,r} \gamma_{m,r}^\alpha a_m \text{Tr}_\xi \rho_{m,r}^\alpha(\xi) \ln \rho_{m,r}^\alpha(\xi), \quad (13)$$

where the summation runs over all clusters of type  $r$  of  $m$  lattice sites included in the maximum cluster or set of maximum clusters which defines the order of the CVM approximation. The  $\gamma_{m,r}^\alpha$  represent a generalization of the ones introduced in the expression of  $U$  and specify the number of clusters per lattice point in superstructure  $\alpha$ . The  $a_m$  are the Kikuchi-Barker coefficients<sup>36,37</sup> whose algebra is discussed elsewhere,<sup>26</sup> and the trace  $\text{Tr}$  is taken over all configurations ( $\xi$ ) of the partial density matrix:<sup>26</sup>

$$\rho_{m,r}^\alpha(\xi) = \frac{1}{2^m} \left[ 1 + \sum_{m',r' \subset m,r} \vartheta_{m',r';m',r'}^\alpha(\xi) \xi_{m',r'}^\alpha \right], \quad (14)$$

where the  $\vartheta^\alpha$  are elements of the so-called “ $\vartheta$ -matrix” or “configuration matrix” expressed as sums of products of the  $\sigma_p$ .<sup>38</sup> In Eq. (14) the summation is over all subclusters ( $m', r'$ ) of the cluster ( $m, r$ ) considered, and  $\xi_{m',r'}^\alpha$  is a multisite correlation function defined as the ensemble average of the product of  $m'$  spinlike variables associated with the  $m'$  points of the cluster of type  $r'$  of the superstructure  $\alpha$ . The main interest of the CVM is to provide a functional form for the configurational free energy that allows a level of approximation for each selected maximum cluster or set of maximum clusters, keeping in mind that questions may arise about the convergence of the CVM free energy towards the exact result when the size of the basic cluster(s) is increased.

When applied to *A15*, the first intuitive approximation which can be considered, besides the single site (or Bragg-Williams) and pair (or Bethe) approximations, makes use of the isosceles triangle which connects sites  $\{1, 2, 3\}$  of Fig. 1(a). This cluster can be used in the CVM context without further approximation with pair interactions extending up to the second-neighbor shell. For the *A15* symmetry, only five correlation functions are necessary to describe the configurational free energy of the ordered state as well as of the disordered state. Indeed, because of the assimilation of the inequivalent sites with site occupancies for this particular superstructure, no distinction is made between complete order and total disorder as far as correlation functions and symmetries are concerned. This remark will remain valid at any level of CVM approximation.










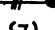





In order to improve the CVM form of the free energy and also to include the effect of further distant pair interactions, one can design a series of approximations based on the analogy between the simple cubic and the *A15* crystalline structures, as shown in Appendix C.<sup>39</sup> The simplest approximation of this kind corresponds to the analog of the pair approximation on a simple cubic lattice and is defined by the combination of three maximum clusters: the two three-point clusters which connect sites  $\{1, 2, 3\}$  and  $\{5, 2, 3\}$ , and the four-point cluster  $\{2, 3, 7, 8\}$  with reference to Fig. 1(a).

The two previous approximations will be called  $T$  (for triangle) and PSC (for pair simple cubic) CVM approximations for future references. We give in Table V the list of correlation functions and the coefficients required to calculate the two contributions (11) and (13) to the free energy of the particular *A15* configuration, for these two CVM approximations.

For completeness, we mention a more general prescription for selecting higher-order approximations based upon a recently developed series of three-dimensional cluster approximations, called the  $C$  and  $T$  hierarchies.<sup>24,40</sup> This procedure presents the advantage over standard CVM of insuring automatically a convergence of the free energy towards the exact results, with the size of the basic clusters, thus avoiding the possibility of getting unphysical results with conventional CVM approximations. In the present study, the  $T$  and PSC-CVM will be compared with the MC results to control the level of accuracy of our CVM results.

Finally, it is of some interest to point out that, within

TABLE V. Parameters required to describe the *T* and PSC clusters in the *A15* ordered configuration. For each approximation, the first column gives the list of subclusters. The *m* and *r* indices specify the correlation functions  $\xi_{m,r}$  and stand for the number of lattice points in the cluster and the type of cluster, respectively. As in Fig. 1(a), the circles and squares refer to sites of the set of chains and of the bcc which form sublattices I and II, respectively; full or empty symbols refer to *A* or *B* species. The length of each edge is specified by conventional bar symbols taken from elementary geometry.

T-CVM					PSC-CVM				
Cluster	<i>m</i>	<i>r</i>	$\gamma$	<i>a</i>	Cluster	<i>m</i>	<i>r</i>	$\gamma$	<i>a</i>
	1	1	2	-5		1	1	2	-5
	2	2	6	-1		2	2	6	0
	3	1	6	-1		3	1	6	-5
	4	1	24	0		4	1	24	0
	5	1	12	1		5	1	24	0
						6	1	6	0
						7	1	12	1
						8	1	24	0
						9	1	6	1
						10	1	6	1

the CVM context, an increase in the size of the basic clusters may become necessary if one wants to introduce further distant interactions. Unfortunately, this can be done to the expense of a dramatic increase in the number of correlation functions (especially for ordered configurations). This problem can be overcome by using a so-called mixed CVM where the correlation functions associated with interactions excluded from the basic clusters are treated in the Bragg-Williams (BW) approximation.<sup>24,40</sup> This procedure will be valid provided the magnitude of the interactions treated in the BW approximation is small compared with the one of interactions taken into account by the basic CVM clusters. In the following, this particular mixed CVM will be referred to as CVM-BW.

## 2. Monte Carlo simulations

Based upon the model Hamiltonian given by Eq. (2), Monte Carlo simulations can be performed to calculate equilibrium thermodynamical properties and ultimately phase diagrams.<sup>27,28,41</sup> In the present study, a model crystal of the *A15* lattice, with a rigid overall cubic shape, was built and helical boundary conditions<sup>42</sup> were applied to it. A sample of  $15^3 \times 8$  atoms has been treated. This size was considered large enough to avoid finite-size effects and to take into account the influence of pair interactions extending around one elementary cubic cell. Computations were performed in the grand-canonical ensemble with optimized Monte Carlo codes which operate at about  $3 \times 10^6$  Monte Carlo steps per site (MCS) per second on a Cray XMP computer. At each temperature and chemical potential, times of 1500 MCS were found sufficient to reach equilibrium. In order to achieve accurate results based on averaging over configurations and to let the system relax in order to prevent the influence of

the initial condition, the first 300 MCS were discarded. Standard thermodynamical integration<sup>28</sup> was applied to calculate the configurational free energy and deduce the entropy contribution, making use of the properties of the system either at infinite temperature or at  $T=0$  K by reference to the ground-state properties presented in Sec. II (see, also, Sec. III).

## B. Phase diagram results with first and second pair interactions

We present in Fig. 12 typical *A15*-based order-disorder phase diagrams for  $\alpha_2=0.4$  and  $\alpha_{s>2}=0.0$ , in both (a) *T* versus chemical potential *h* and (b) *T* versus concentration *c*, representations. The value of  $\alpha_2$  was chosen in order to be in a region of the ordering map of Fig. 4(b) where the three phases *F*, *A15*, and *X* exist at  $T=0$  K. Because the pair interactions which enter the statistical model [see Eq. (2)] are concentration independent, the phase diagram is symmetric, in both representa-

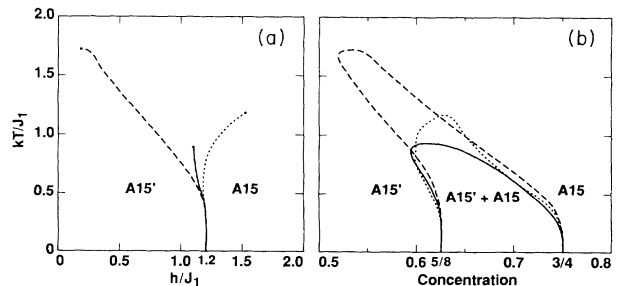


FIG. 12. Prototype phase diagrams in the grand-canonical (a) and the canonical (b) representations, for  $\alpha_2=0.4$  and  $\alpha_{s>2}=0.0$ . Comparison between BW (dashed curve), T-CVM (dotted curve), and Monte Carlo (solid curve) results.

tions around  $h=0$  or  $c=\frac{1}{2}$ . In  $\{J_1, J_2\}$ , both  $T$  and PSC-CVM approximations produce almost indistinguishable results in satisfactory overall agreement with the MC results. As observed for simple lattices, the CVM overestimates the maximum temperature of the

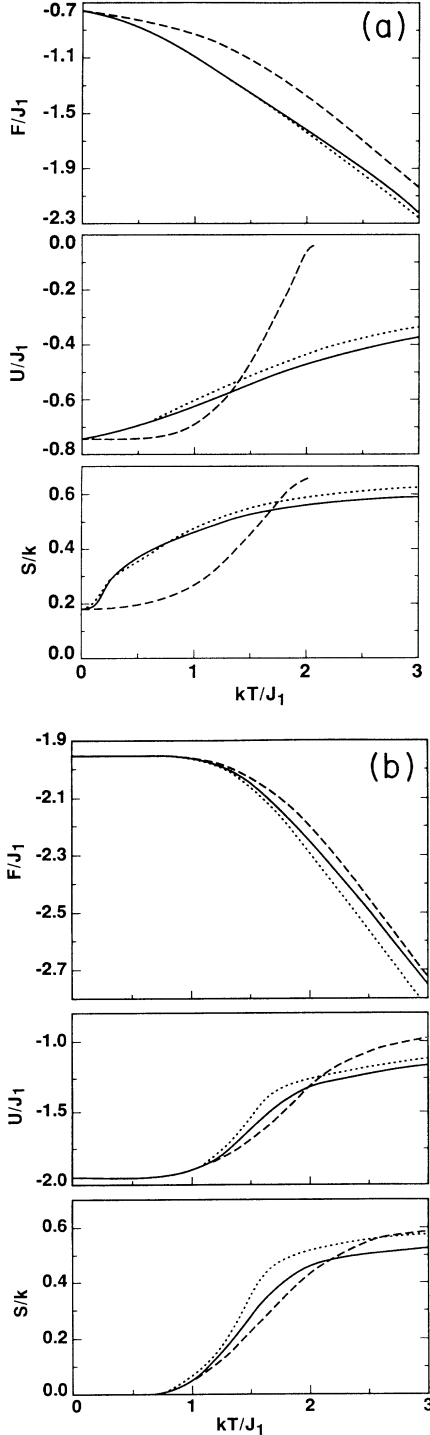


FIG. 13. Free energy (top), internal energy (middle), and entropy (bottom) vs temperature, at (a)  $h=0$  and (b)  $h=3$ , for  $\alpha_2=0.4$  and  $\alpha_{s>2}=0.0$ . Comparison between BW (dashed curve), T-CVM (dotted curve), and Monte Carlo (solid curve) results.

two-phase region. Although the Bragg-Williams treatment is not quantitatively correct (except at low temperature, see Appendix B), it provides a qualitative picture in good agreement with the ones deduced from higher-order approximations. In Fig. 13, we summarize this comparative study by plotting the configurational energy, the free energy, and the entropy as a function of temperature, at  $h=0$  ( $c=\frac{1}{2}$ ) and  $h=3$ , where  $A15'$  (of  $X$ -type short-range order) and  $A15$ , respectively, are stable. In the  $T$  versus  $h$  representation [see Fig. 12(a)], the first-order line ends at a critical second-order point. Because the chains of the  $X$  phase disorder at  $T \neq 0$  K, the disordered  $X$  phase (or  $A15'$ ) shares the same symmetry as the  $A15$  phase and therefore the  $A15'-A15$  equilibrium is similar to a “liquid-gas” transition on the  $A15$  lattice, quite comparable to the  $F(B)-F(A)$  line of the fcc-Ising model with ferromagnetic first pair interactions ( $J_1 < 0$ ). One can also remark that there is no order-disorder transition at the composition  $A_3B$ . Stated another way, any long-range-order (LRO) parameter  $\eta$  (and more generally any correlation function) which can be defined for the  $A15$  superstructure tends smoothly towards the value it should have when complete disorder takes place at infinite temperature. This property is illustrated in Fig. 14 where the LRO parameter given by  $\eta_{A15} = \frac{1}{2}(\langle \sigma_I^{(2)} \rangle - \langle \sigma_{II}^{(1)} \rangle)$  is plotted as a function of temperature for various values of  $\alpha_2$ , at  $c = \frac{3}{4}$ .  $\langle \sigma_\alpha^{(i)} \rangle$  stands for an ensemble average value of the point correlation function of site ( $i$ ), by reference to Fig. 1(a), on sublattice  $\alpha$ .

Although the phase diagram only exhibits  $A15$ , the short-range order (SRO) is expected to vary dramatically with composition. Indeed, around  $c = \frac{5}{8}$  and  $c = \frac{3}{4}$ , the SRO will reflect the existence at zero temperature of the  $X$  and  $A15$  phases, respectively (see Sec. V A). This effect can be seen theoretically if one plots some typical cluster probabilities, as expressed by Eq. (14), as a function of concentration. Indeed, by contrast to BW calculations, the minimization of the CVM free-energy functional gives values for the multiplet correlation functions, up to the size of the maximum cluster(s) of the CVM approximation, hence providing a real space picture of SRO.<sup>43</sup>

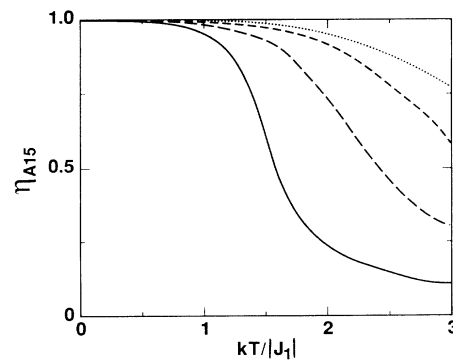


FIG. 14. Long-range order parameter vs temperature, of the  $A15$  configuration (see text for a definition of  $\eta_{A15}$ ), at  $c = \frac{3}{4}$ , for various values of  $\alpha_2$ :  $-0.4$  (dotted curve),  $+0.4$  (solid curve),  $+0.5$  (long-dashed curve),  $+0.6$  (dashed curve). Results obtained from T-CVM, with  $\alpha_{s>2}=0.0$ .

Results for the isosceles triangle cluster probabilities, together with the LRO parameter  $\eta_{A15}$  defined above, are plotted in Fig. 15 as a function of concentration for  $\alpha_2=0.4$ , at low and relatively high temperatures (where  $A15$  and  $X$  exists at  $T=0$  K), and for  $\alpha_2=0.6$  (where only  $A15$  is stable) for comparison.

Monte Carlo simulations, supposedly leading to exact results, show that the hard-sphere description presented in Appendix B is correct, i.e., no transition line exists for the  $F(A)-A15(A_3B)$  equilibrium around  $h_c=12J_2$  ( $h_c=4.8$  for  $\alpha_2=0.4$ ). We display in Fig. 16, the internal energy and the specific heat  $C$  in the low-temperature re-

gime, at  $h=4.7$  ( $\alpha_2=0.4$ ). As analyzed in Appendix D, the maximum in  $C(T)$  is not related to any particular transition but instead, to a Schottky anomaly. This behavior is the natural consequence of the saturation of very low-energy excitations, well isolated from higher-energy ones, whose existence is intimately related to the presence of a superdegenerate point at  $h_c=12J_2$ . Precisely at  $h_c$ , these excitations have zero energy (they already exist at  $T=0$  K) and the heat capacity does not show a local maximum at low temperature. This situation compares with the one encountered for the superdegenerate points at  $h_c=4J_1$  and  $12J_1$  for an fcc lattice

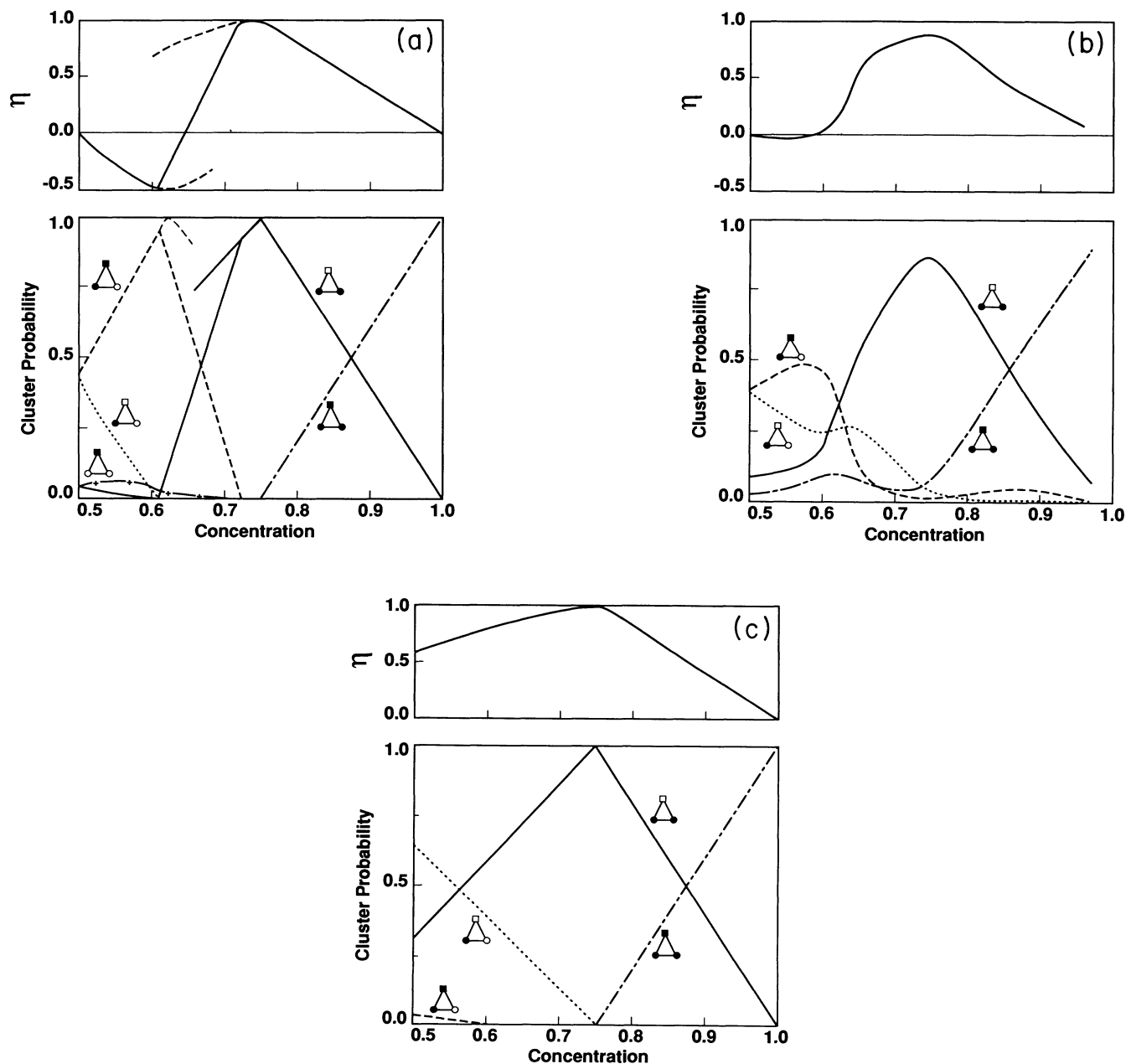


FIG. 15. Concentration dependence of the most significant cluster probabilities [isosceles triangle  $\{1,2,3\}$  of Fig. 1(a)] for  $\alpha_2=0.4$ ,  $\alpha_{s>2}=0.0$ , and  $kT/J_1=0.5$  (a),  $kT/J_1=1.2$  (b); for  $\alpha_2=0.6$ ,  $\alpha_{s>2}=0.0$ , and  $kT/J_1=0.85$  (c). The top part of each figure indicates the evolution of the long-range order parameter  $\eta_{A15}$  with concentration. Results obtained from  $T$ -CVM.

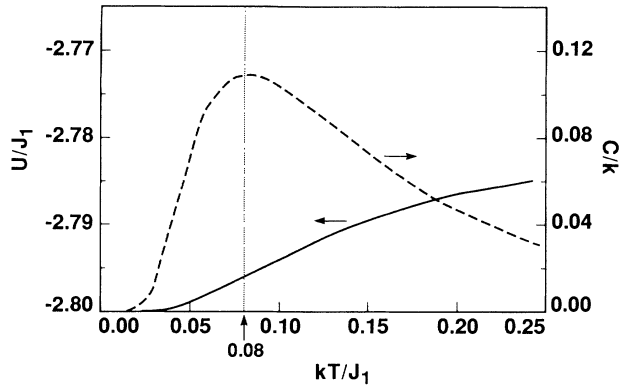


FIG. 16. Internal energy (solid curve) and heat capacity (dashed curve) vs temperature, for  $\alpha_2=0.4$  and  $\alpha_{s>2}=0.0$ , as computed from Monte Carlo simulations at  $h=4.7$ .

with antiferromagnetic first pair interactions.<sup>24,44</sup> Note that the location of the maximum of the specific heat in Fig. 16 compares satisfactorily with the estimated value given in Appendix D.

For completeness, prototype phase diagrams for  $\alpha_2=0.3$  are presented in Fig. 17. These results confirm and complete the low-temperature analysis performed in Sec. III A.

### C. Phase diagram results in $J_1, J_2$ , and $J_7 < 0$

The PSC-CVM approximation was used to take properly into account the effect of first and second pair interactions and was combined with a BW treatment of the seventh pair interactions (PSC-CVM-BW; see discussion in Sec. IV A 1). The resulting prototype phase diagram for  $\alpha_2=0.4$  and  $\alpha_7=-0.01$  is displayed in Fig. 18. The set of interactions was selected to stabilize the  $X$  phase (i.e.,  $X_1$ , because  $J_7 < 0$ ; see Sec. II C) at finite temperature and to remove the degeneracies associated with the  $F$ - $A15$  and  $X$ - $\bar{X}$  phase equilibria. About the remarkable features of this phase diagram [see Fig. 18(a)], one can note the existence of three first-order lines which end at critical second-order points. The  $X(A_5B_3)$ - $\bar{X}(A_3B_5)$  line can be viewed as a “liquid-gas” transition on sublattice II, i.e., there is no real difference between the  $X$  and

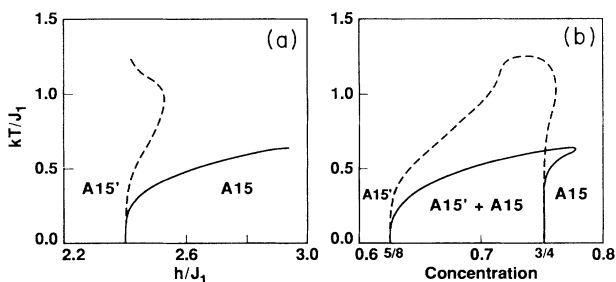


FIG. 17. Prototype phase diagrams in the grand-canonical (a) and the canonical (b) representations, for  $\alpha_2=0.3$  and  $\alpha_{s>2}=0.0$ . Comparison between BW (dashed curve) and  $T$ -CVM (solid curve) results.

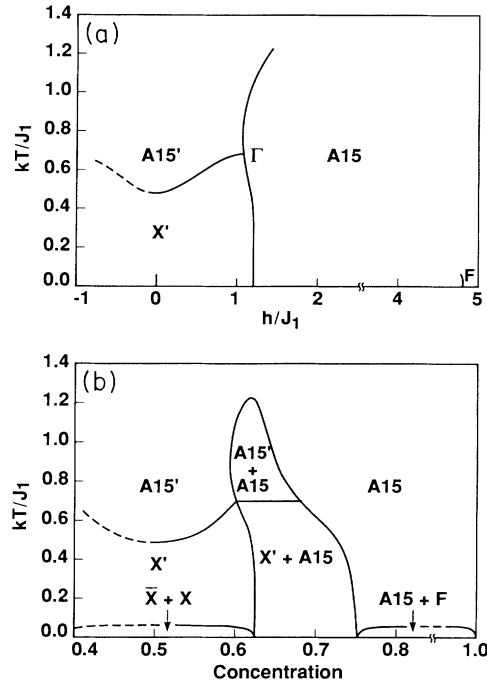


FIG. 18. Prototype phase diagrams in the grand-canonical (a) and the canonical (b) representations for  $\alpha_2=0.4$  and  $\alpha_7=-0.01$ , as obtained from PSC-CVM-BW.

$\bar{X}$  phases. In other words, following a path which goes around the  $X$ - $\bar{X}$  line, one of the phases transforms continuously into the other, hence the notation  $X'$  hereafter. The height of this line goes continuously towards zero with  $J_7$ , as illustrated in Fig. 19. Similar comments apply for the  $F(A)-A15(A_3B)$  line. Finally for the  $A15(A_3B)$ - $X(A_5B_3)$  equilibrium, we have a standard first-order line up to a tricritical point denoted  $\Gamma$  in Fig. 18(a). This point terminates a second-order line associated with the disorder of the “antiferromagnetically” ordered linear chains of the  $X'$  phase. This second-order transformation is illustrated in Fig. 20 where the LRO parameter of the  $X$  phase, given by  $\eta_X = \frac{1}{2}(\langle \sigma_1^{(2)} \rangle - \langle \sigma_1^{(3)} \rangle)$  (see definition of the  $\langle \sigma_\alpha^{(i)} \rangle$  in previous section), is plotted as a function of temperature, at  $c = \frac{1}{2}$  ( $h=0$ ), with  $\eta_{A15}(T)$ , at  $c = \frac{3}{4}$ , for comparison. One should notice in Fig. 20 that sublattice II of  $A15$  disorders at a faster rate, as a function of temperature, than

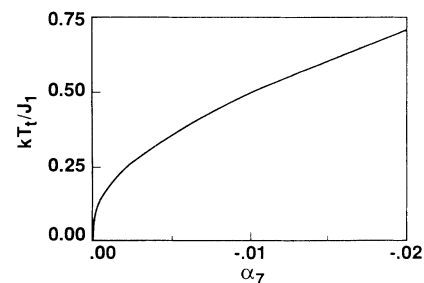


FIG. 19. Transition temperature  $T_i$  associated with the transformation  $X'$  to  $A15'$  (see Fig. 18) as a function of  $\alpha_7$ , for  $\alpha_2=0.4$ , and as obtained from PSC-CVM-BW.

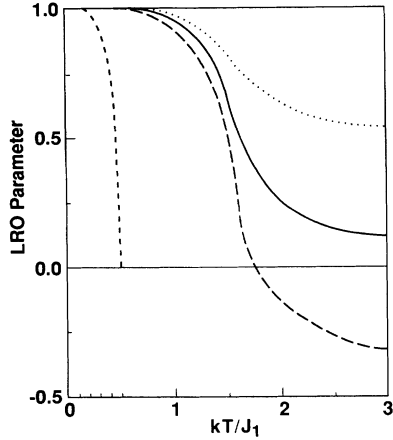


FIG. 20. Long-range order parameter  $\eta_X$  (short-dashed curve) at  $c = \frac{1}{2}$ , and  $\eta_{A15}$  (solid curve),  $\langle \sigma_I^{(2)} \rangle$  (dotted curve), and  $-\langle \sigma_{II}^{(1)} \rangle$  (long dashed curve) at  $c = \frac{3}{4}$ , vs temperature for  $\alpha_2 = 0.4$  and  $\alpha_7 = -0.01$ , as obtained from PSC-CVM-BW.

sublattice I, and that  $\langle \sigma_I^{(2)} \rangle = \langle \sigma_{II}^{(1)} \rangle = 2c - 1$  ( $= \frac{1}{2}$ ) at infinite temperature.

From our study, which has proved the fundamental richness in examining phase stability properties of alloys based on nonsymmorphic complex lattices, we can draw the following conclusions. Below the stoichiometric composition  $c = \frac{3}{4}$ , a two-phase field involving the  $X$  and  $A15$  superstructures may exist until  $c = \frac{5}{8}$  where the  $X$  phase is found stable, for a regime of interactions such that  $\frac{1}{4} \leq \alpha_2 \leq \frac{1}{2}$  and  $\alpha_7 \neq 0$ . Meanwhile our findings suggest that the  $X$  phase should be stable at relative low temperature. Indeed, a  $J_1$  of the order of 50 meV, as estimated

from electronic structure calculations,<sup>19,22</sup> leads to a value of the critical temperature of the mixed  $A15'(X)$ - $A15$  region of the order of 700 K, which may explain why the  $X$  phase has not yet been identified experimentally.

## V. DISCUSSION

First, we present further details about the crystallographic characterization of the  $X$  phase, by comparison with the  $A15$  phase, in terms of typical as-computed diffraction patterns and SRO diffuse scattering intensities. We also briefly discuss the electronic structure properties of transition-metal alloys possessing the  $X$  type of order in a tight-binding framework. Then we present a list of the possible candidates which may show the  $X$  phase, and comment on the other complex phases which may compete around the composition  $A_5B_3$  with the predicted  $X$  phase, before summarizing our results.

### A. Characterization of the $X$ phase

If a single variant of the  $X$  phase can exist, its diffraction pattern must exhibit some typical (but possibly weak) peaks at the (100), (001), (111), (221), (212), . . . positions (in units of  $2\pi/a$ , where  $a$  is the  $A15$  lattice parameter) which are not found for the  $A15$  ordered state. Indeed, if  $f_A$  and  $f_B$  are the atomic factors of diffusion of both species for the electrons, the kinematic structure factors for the  $A15$  and  $X$  superstructures are given by

$$F_{A15}(h, k, l) = f_B [1 + e^{i\pi(h+k+l)}] + 2f_A [e^{i\pi h} \cos(\Pi/2)k + \text{c.c.}],$$

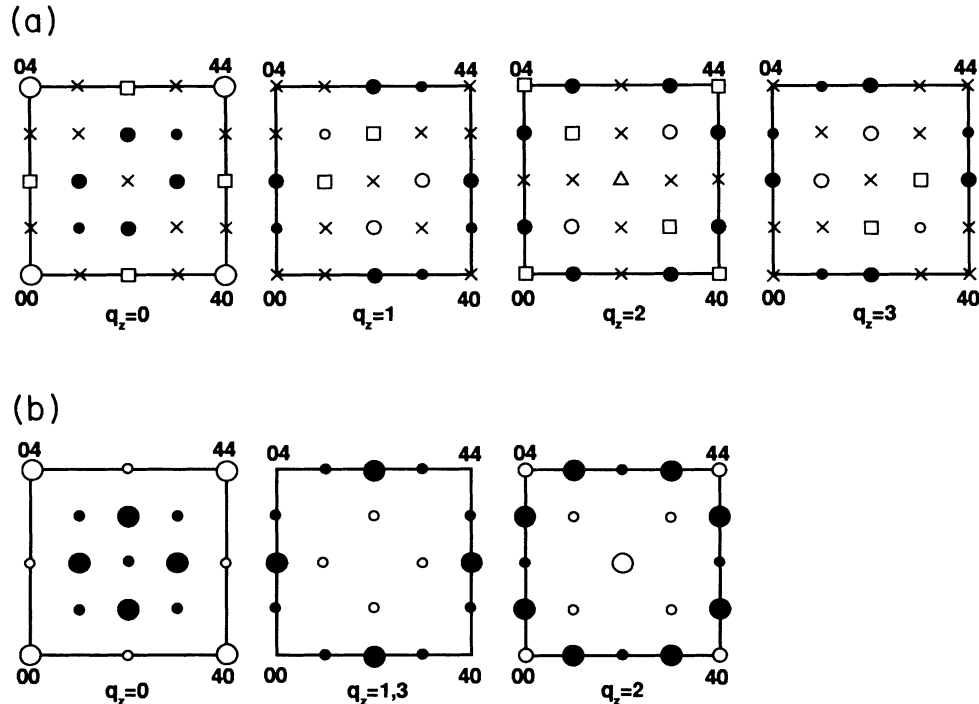


FIG. 21. Typical diffraction patterns and their indexations for the  $X$  (a) and  $A15$  (b) configurations. The hierarchy of intensities are (a) for  $X$ :  $\circ > \square > \bullet > \blacklozenge > \triangle > \diamond > \blacklozenge > \times$ , and (b) for  $A15$ :  $\circ > \square > \bullet > \blacklozenge > \diamond > \bullet$ .

$$F_x(h, k, l) = f_B [e^{i(\pi/2)(2h+k) + \psi}] + f_A [e^{i\pi(h+k+l)} + e^{i(\pi/2)(2h-k) + \psi}],$$

where  $h, k$  and  $l$  are the components (in units of  $2\pi/a$ ) of the reciprocal vector  $\mathbf{q}$ . Thus, additional peaks with intensity  $I_{hkl}$  proportional to  $|F(h, k, l)|^2$  will result for the  $X$  phase, as illustrated in Fig. 21. More suitable, SRO diffuse-scattering-intensity measurements with x rays or neutrons, above the domain of existence of the  $X$  phase [see Fig. 18(b)] should show maxima of diffuse intensity,  $I_{\text{SRO}}$ , at the aforementioned positions. These maxima should be relatively easy to probe because of the second-order character of the transition  $X'$  to  $A15'$  (see comment in Sec. IV C). By definition,  $I_{\text{SRO}}$  is given by

$$I_{\text{SRO}} = \langle |\sigma(q)|^2 \rangle - |\langle \sigma(q) \rangle|^2,$$

where  $\langle \sigma(q) \rangle$  and  $\langle |\sigma(q)|^2 \rangle$  are the Fourier transforms of the point  $\langle \sigma(p) \rangle$  and pair  $\langle \sigma(p)\sigma(p') \rangle$  correlation functions. It is then easy to extend the known CVM expression of  $I_{\text{SRO}}$  (Ref. 43) to a nonsymmorphic lattice. The results are presented in Fig. 22. The PSC-CVM-BW approximation, with  $\alpha_2=0.4$  and  $\alpha_7=-0.01$ , has been used to compute  $I_{\text{SRO}}$ , at relatively high temperature  $kT/J_1=2.0$  [see phase diagram of Fig. 18(b)], in the (001) plane with  $q_z=1.0$ , where the maximum difference between the SRO's of  $X$  type [ $h=1.0$ ; Fig. 22(a)] and of  $A15$  type [ $h=3.5$ , Fig. 22(b)] becomes apparent. Quantitatively, these results are almost identical to the ones

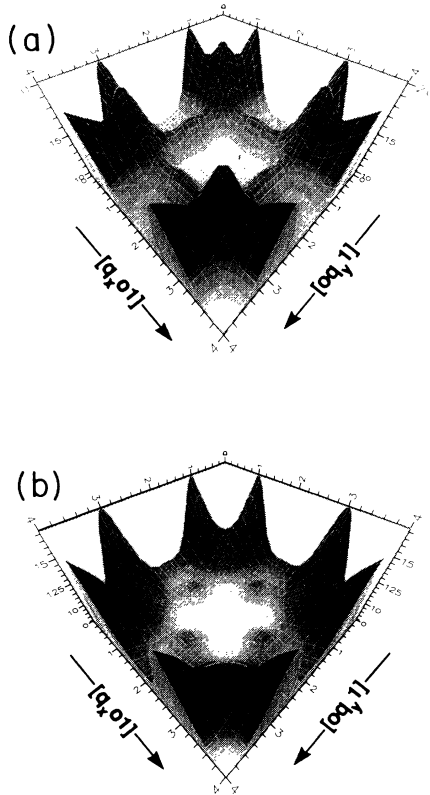


FIG. 22. SRO diffuse scattering intensity in the (001) plane with  $q_z=1.0$  as computed with the PSC-CVM-BW.  $\alpha_2=0.4$ ,  $\alpha_7=-0.01$ ,  $kT/J_1=2.0$ , and  $h/J_1=1.0$  (a),  $h/J_1=3.5$  (b).

obtained in the simple  $T$ -CVM approximation with only first and second pair interactions. This fact, once again, proves that  $J_7$  is only important to describe the LRO of  $X$  type but has little effect on the existence of the SRO of this type. It should be emphasized that because no real order-disorder transformation takes place in the  $A15(A_3B)$  superstructure, the SRO diffuse peaks are located at the Bragg positions of the  $A15$  crystalline structure, as for an alloy which would have a tendency to phase separate. As a consequence the SRO only manifests itself as a diffuse broadening at the Bragg locations.

### B. Electronic structure properties of the $X$ phase

The electronic structure and stability properties of the  $X$  phase, at  $T=0$  K, are examined in the framework of the tight-binding-coherent potential approximation-generalized perturbation method (TB-CPA-GPM).<sup>19,22</sup> This preliminary study primarily applies to transition-metal alloys for which  $d$ -valence electrons play a major role in explaining their stability properties. The TB Hamiltonian and the electronic parameters have already been discussed in a previous study.<sup>19</sup> Typical densities of states (DOS's) for both fully ordered configurations,  $A15(A_3B)$  and  $X(A_5B_3)$  ( $X_1$ , more precisely: see Fig. 6) are displayed in Fig. 23 with their respective  $d$ -band filling (or average number of  $d$  electrons). The DOS's

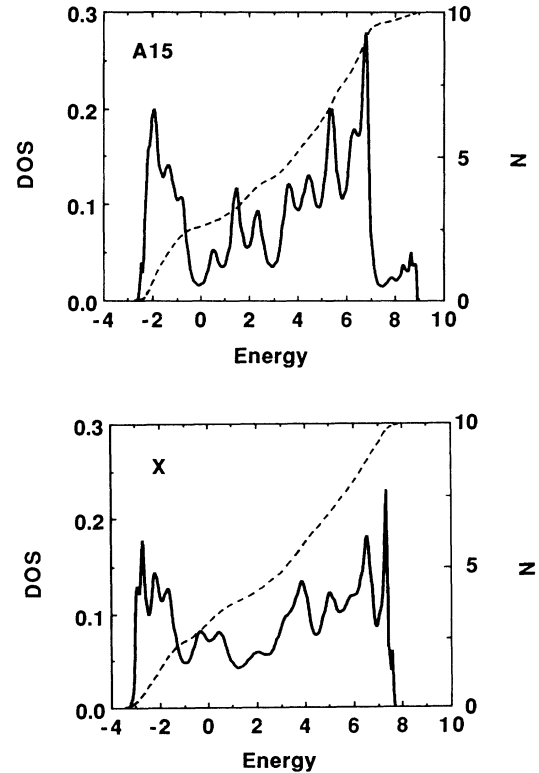


FIG. 23. Total DOS (solid curve; in arbitrary units) and average band filling  $N$  (dashed curve) as computed in the tight-binding framework with a diagonal disorder parameter of 0.8 (see text), for both fully ordered  $A15(A_3B)$  and  $X(A_5B_3; X_1)$  of Fig. 6) configurations.

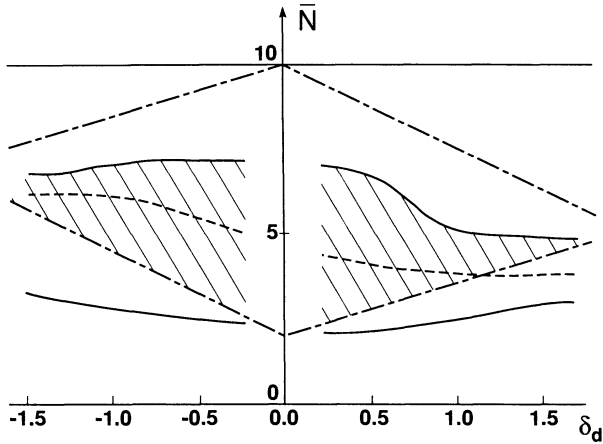


FIG. 24. Theoretical structural map as obtained from tight-binding calculations indicating the probable domains of stability of the  $X$  phase within the solid lines, with the maximum of stability mentioned by dashed curves. Real transition-metal alloys occur between the chain curves (corresponding to  $2 \leq N_A, N_B \leq 10$ ).

were calculated with the recursion technique<sup>45</sup> from the continued fraction expansion of the one-electron Green function, exact up to the 18th level. This accuracy requires clusters of 31445 and 31727 atoms centered around sites of sublattice I and II, respectively. The diagonal disorder,  $\delta = (\varepsilon_A - \varepsilon_B) / \bar{W}$  where  $\varepsilon_i$  is the on-site energy of species  $i$  and  $\bar{W}$  is the mean half width of the  $d$  bands of the pure metals, is equal to 0.8 to reproduce a case of intermediate disorder effect. Figure 23 shows that the total DOS of the  $X$  phase has some parentage with the one of the  $A15$  phase, especially with regards to the low-energy part of the DOS, in a region of band filling less than five  $d$ -valence electrons. Meanwhile, distinctions have to be made at high band filling in association, particularly, with the chemical order which takes place along the chains in the  $A15$  and  $X$  configurations. As for the stoichiometric composition  $A_3B$ ,<sup>19</sup> it has been checked that the effective pair interactions, calculated in the GPM approach at  $c = \frac{5}{8}$ , converge rapidly with neighbor distance, and multisite interactions are indeed negligible when compared with pair interactions. These results support the basic assumptions made in the present study. Finally, the band term contribution to various energetic properties, including mixing energies from TB-CPA and ordering energies as expressed in the GPM framework (see Ref. 19 for a definition of these quantities) was estimated as a function of the diagonal disorder  $\delta$ , and of the average  $d$ -band filling  $\bar{N}$ , at fixed concentration  $c = \frac{5}{8}$ . In practice, there is a relation between  $\Delta N = N_B - N_A$  and  $\delta$ . In this work, we assume  $\varepsilon_A - \varepsilon_B = K \Delta N$ , with  $K \approx 1$  eV, which is known to be a reasonable approximation, at least for elements belonging to the same transition series. Therefore if  $\delta$  and the concentration are held fixed,  $\bar{N}$  can be changed by varying separately  $N_A$  and  $N_B$  while keeping  $\Delta N$  constant. In addition, the regions of stability corresponding to small values of  $\delta$ , and therefore of  $\Delta N$ , will be omitted since they would correspond to very weak ordering tendencies,

presumably not observable experimentally. Including these constraints, the domains of possible existence of the  $X$  type of order are indicated by the hatched regions in the ground-state structural map of Fig. 24. The physical bounds due to the constraint  $2 \leq N_A, N_B \leq 10$  have been indicated by the mixed lines, whereas the dashed lines locate the maximum value of the ordering energy of the  $X$  phase, as a function of  $\delta$ . More complete versions of its counterpart at  $c = \frac{3}{4}$  have been discussed in detail in Ref. 19. This study confirms the potential existence of the  $X$  phase for an average number of  $d$  electrons less than 6. As for the case  $c = \frac{3}{4}$ , the stability of the  $X$  phase is primarily driven by a structural effect. In other words, the relative stability energy of the  $X$  phase does not drastically depend on the atomic configuration, i.e., on  $\delta$  as seen in Fig. 24. It would be interesting to extend this comparative study to include other competing complex phases as the ones discussed in the next section.

### C. Experimental implications

With regard to experiment, one might suggest some systems which show an  $A15$  crystalline structure in a broad range of concentration where the  $X$  phase could be detected. From Table II, the following transition-metal (TM) alloys are of potential interest: Ti-Pt, V-(Rh, Ir, or Pt), Nb-(Os, Ir, or Au), Cr-Ir, and the special cases of Mo-Tc ( $c_{\text{Mo}} \sim 0.46$ ) and V-Os ( $c_{\text{V}} \sim 0.52$ , at high temperature). One might also consider among the TM-non-TM alloys: V-Ga, Nb-Al, and Mo-Al. For all these alloys, a secondary ion beam codeposition of metallic alloy thin films<sup>46</sup> seems to be the most appropriate technique to reveal the  $X$  phase in a metastable state, if not in a stable state.

It is interesting to note that for  $c < \frac{3}{4}$ , the  $A15$  crystal-

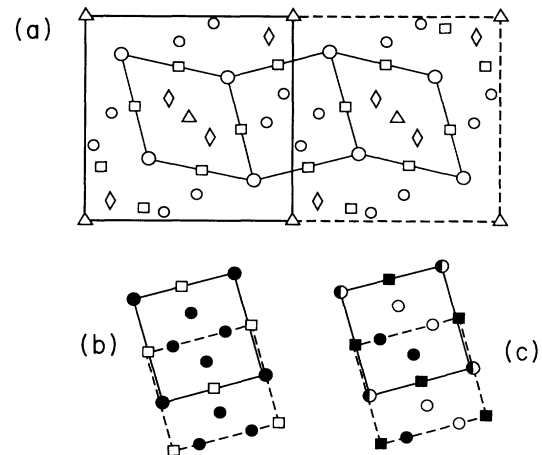


FIG. 25. (a) Projection along the  $c$  axis of two unit cells of the  $\sigma$  phase:  $\Delta, \diamond, \circ, \square, \circ$  refer to sites of sublattices  $A, B, C, D,$  and  $E$ , respectively. The rhombi and the square delimited by thin lines indicate the two kinds of building blocks ( $Z$  and  $A15$ , respectively) constituting the  $\sigma$  phase. (b) and (c) specify the chemical order on various sites of the  $\sigma$  phase constrained by a local configuration of the  $A15$  ( $A_3B$ ) or  $X$  ( $A_3B_3$ ) type, respectively. Full or empty sites in (b) and (c) refer to  $A$  or  $B$  species, respectively.



TABLE VI. Site occupancy per sublattice of the  $\sigma$ -phase standard configuration ( $A+B$  denotes a random mixture of  $A$  and  $B$  species) to be compared with the ones associated with local order of  $A15$  and  $X$  types.  $\mu$  and CN refer to sublattice multiplicity and coordination number, respectively.

Sublattice	$\mu$	CN	$\sigma$ occupancy	Local order: $A15$ occupancy	Local order: $X$ occupancy
$A$	2	12	$B$		
$B$	4	15	$A$		
$C$	8	14	$(A+B)$	$A$	$A_{1/2}+B_{1/2}$
$D$	8	12	$B$	$B$	$A$
$E$	8	14	$(A+B)$	$A$	$A_{1/2}+B_{1/2}$

line structure competes with the  $D8_b$  (or  $\sigma$ , of FeCr type) for TM alloys,  $D8_m$  (of  $W_5Si_3$  type) or  $D8_8$  (of  $Mn_5Si_3$  type) for TM-non-TM alloys.<sup>17</sup> It is well known that all the Frank-Kasper phases based on tetrahedrally close-packed structures can be described in terms of simple building blocks (belonging themselves to this class of structures), or prototiles, which are the  $A15$ ,  $Zr_4Al_3$  (or  $Z$ ) and one of the Laves phases ( $C14$ ,  $C15$ , or  $C36$ ) units.<sup>47,48</sup> In particular, the tetragonal structure ( $D_{4h}^{14}$  or  $P4_2/mnm$ ) of the  $\sigma$  phase, which possesses 30 atoms per unit cell, can be described either by its five sublattices, commonly named  $A$  to  $E$ , with respective coordination number CN12, CN15, CN14, CN12, and CN14,<sup>9,13</sup> or by considering its two building blocks  $A15$  and  $Z$ .<sup>47,48</sup> Because the  $\sigma$  phase usually exists in a broad range of concentration, it would be interesting to examine in more detail the chemical order which develops in particular on the so-called  $C$ ,  $D$ , and  $E$  sublattices which form the  $A15$  building blocks [see Fig. 25(a)]. If the local order in the  $\sigma$  phase resembles the one described either by the  $A15$  ( $A_3B$ ) or the  $X$  ( $A_5B_3$ ) superstructures, then specific site occupancies are expected, as illustrated in Figs. 25(b)

and 25(c). We give in the first column of Table VI, the standard site occupancy for each sublattice of the  $\sigma$  phase<sup>9,13</sup> with, in the next two columns, the site occupancies constrained by a local order of  $A15$  or  $X$  type. In the latter case, note that the chains of the  $E$  sublattice, along the  $c$  axis, are alternatively occupied by  $A$  and  $B$  species [see Fig. 25(c)], hence the notation  $A_{1/2}+B_{1/2}$  in Table VI. If one assumes that the occupancy of the  $A$  and  $B$  sublattices is not affected by a local order of  $A15$  or  $X$  type, then both configurations would lead to the same alloy composition  $A_2B$ . Alloys of interest include V-Co, V-Ni, and Nb-Os ( $A=V$  or Nb), which are found stable in the  $\sigma$  composition range: 46–72 at. % V, 44–75 at. % V, and 55–65 at. % Nb, respectively.

Contrary to the  $\sigma$  phase,  $D8_m$  and  $D8_8$  usually exist as line compounds, and geometrical factors cannot be ignored. Meanwhile, in the case of  $D8_m$  (of  $W_5Si_3$  type), a complex tetragonal structure ( $D_{4h}^{18}$  or  $I4/mcm$ ) with 32 atoms per unit cell, a so-called Hyde rotation of  $\Pi/4$  (Refs. 48 and 49) transforms this structure back into an  $A15$  one, as shown in Fig. 26. Hence, assuming that the  $D8_m$  configurational order is preserved during this col-

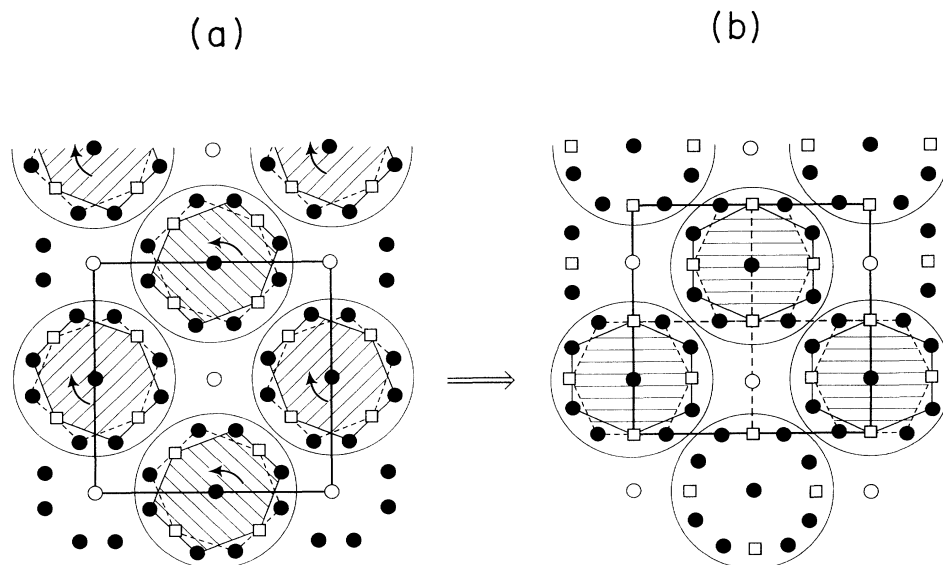


FIG. 26. (a) Projection along the  $c$  axis of the  $D8_m$  crystalline structure (of  $W_5Si_3$  type). One unit cell is specified within the thick solid line. The full and empty circles and empty squares refer to the three inequivalent sites of the structure occupied by  $A$  (full symbols) and  $B$  (empty symbols) species (final composition:  $A_5B_3$ ). By applying a Hyde rotation, i.e., a collective rotation of the sites inscribed in each cylinder, of  $\pi/4$  in a direction indicated by the arrow, the transformed structure represented in (b) is described by four  $A15$  unit cells.

lective atomic motion, an ordered configuration based on four A15 unit cells results [see Fig. 26(b)]. This superstructure reveals an A15 order except for a set of chains along one cubic direction which are alternatively fully occupied by A or B species. This configuration, not found in the present ground-state analysis, demonstrates that more subtle interplay between geometrical factors and ordering mechanism can take place in nature.

## VI. CONCLUSION

We have investigated order-disorder phenomena in A15-based alloys on a theoretical ground and predicted the possible existence of additional ordered configurations. Prototypical phase diagrams were studied in detail. For those alloys which display an A15 structure in a broad range of concentration, our findings suggest that it would be interesting to carry out a careful study of SRO diffuse scattering intensities as obtained by x rays or neutrons, in an attempt to reveal experimentally the X phase which may exist at low temperature in a metastable state, if not in a stable one. Experiments are underway to substantiate such findings. Our analysis also suggests experiments to be performed on competing phases such as the  $\sigma$  phase where local order is expected to mimic the one described on an A15 lattice. In the meantime, we have shown that the existence of crystallographically inequivalent sites in a lattice produces a number of peculiarities, as far as thermodynamics is concerned, a remark which should apply to similar cases such as interstitial ordering in alloys.

Finally, the extension of this study to other tetrahedrally close-packed structures which are stabilized mostly for electronic reasons, should improve our understanding on the interplay between geometrical factors and configurational effect and its significance in the formation of complex phases.

## ACKNOWLEDGMENTS

The authors thank Dr. F. Ducastelle and Dr. A. F. Jankowski, and Professor R. Kikuchi for stimulating discussions. This work was supported by the U.S. Department of Energy at the Lawrence Livermore National Laboratory under Contract No. W-7405-ENG-48. One of us (A.F.) would like to thank LLNL, where part of this work was done, for its financial support and hospitality.

## APPENDIX A

Let us consider the  $\mu_n$  configurations on a linear chain of length  $n$  with the only two possible pair occupancies AA and AB.  $\mu_n$  is given by the sum of  $\mu_n^A$  and  $\mu_n^B$ , the number of these chains which end by an A and B species, respectively:

$$\mu_n = \mu_n^A + \mu_n^B.$$

By adding an extra atom, we have

$$\mu_{n+1} = 2\mu_n^A + \mu_n^B = \mu_n + \mu_n^A$$

with  $\mu_n^A = \mu_{n-1}^A + \mu_{n-1}^B = \mu_{n-1}$ . Therefore we have the re-

currence:

$$\mu_{n+1} = \mu_n + \mu_{n-1}.$$

The solution of the form  $\mu_n \sim x^n$  leads to the equation

$$x^2 - x - 1 = 0$$

and  $\mu_n = \tau^n$ , where  $\tau$  is the golden number  $\tau = (1 + \sqrt{5})/2$ .

Thus, for a chain of length  $L$ , there are  $2L$  sites, and in an A15 structure, because the  $3L^2$  chains are independent, the degeneracy  $d$  is given by  $d = (\tau^{2L})^{3L^2} = \tau^{6L^3}$  and the residual entropy  $S$  by

$$S = \lim_{L \rightarrow \infty} \frac{1}{8L^3} \ln \tau^{6L^3},$$

that is,  $S = \frac{3}{4} \ln \tau \sim 0.3609$ .

## APPENDIX B

Although standard low-temperature expansion analysis does not apply in the neighborhood of a superdegenerate point, it is still possible to establish an analogy with the so-called hard-sphere problem to get information on the topology of phase diagrams near this kind of point.<sup>24,32</sup>

If  $h_c$  is the chemical potential at this point, the Hamiltonian is rewritten as

$$H = H_c - \Delta h \sum_n \sigma_n,$$

where  $H_c$  is the Hamiltonian associated with  $h_c$  and  $\Delta h = h - h_c$ .

The partition function  $Z$ , near  $h_c$ , takes the form

$$Z = \sum' \exp \left[ \beta \Delta h \sum_n \sigma_n \right],$$

where the first summation is restrained to the ground-state configurations of  $H_c$  and the origin of energy is readjusted to the ground-state energy of  $H_c$ . As expected for a superdegenerate point,  $Z$  and all the derived thermodynamical functions depend on  $T$  and  $h$  only through  $\Theta = \beta \Delta h$ . This problem can be reformulated in the language of "lattice gas" by replacing the spinlike variables by their corresponding occupation numbers,  $p_n = (1 - \sigma_n)/2$ , and  $Z$  becomes

$$Z = z^{-N/2} \sum' z^n, \quad z = e^{-2\Theta},$$

where  $n$  is the number of occupied sites (i.e., associated with nonzero occupation numbers) in a given configuration.

This expression corresponds to a partition function of a lattice gas with constraint (cf. prime in the summation) and  $z$  acts as an activity. Therefore the limit of  $Z$ , when  $T$  and  $h$  tend, respectively, towards 0 and  $h_c$ , is equivalent to the solution of a lattice-gas problem if  $\Theta$  remains constant. In other words, in the plane  $(T, h)$ , the limits  $T \rightarrow 0$  and  $h \rightarrow h_c$ , along a line of slope  $\Theta$  is equivalent to a lattice-gas solution with activity  $z = e^{-2\Theta}$ .

Contrary to a nonsuperdegenerate point for which  $T \rightarrow 0$  depends only on the sign of  $\Theta$ , this limit depends explicitly and uniquely on the angle  $\Theta$  in the case of a su-

perdegenerate point. Accordingly, the concentration  $c(\Theta)$  decreases continuously with  $\Theta$  (except for specific values  $\Theta_c$  if first-order transition lines emerge from the superdegenerate point), because an infinity of stable states are available at  $h = h_c$ . On the contrary  $c(\Theta)$  takes two values, those corresponding to the two ground states, in the case of a non-superdegenerate point.

It is easy to show that the entropy  $s(\Theta)$ , in the limit  $T \rightarrow 0$ , along a line of slope  $\Theta$  is maximum when  $\Theta = 0$ , i.e., when the superdegenerate point is approached vertically.

As an application, consider the case of the  $F(A)-A15(A_3B)$  equilibrium, with first- and second-nearest pair interactions,  $J_1$  and  $J_2$ , only. The ground-state energies per unit cell are given by

$$E_F = -8h + 6J_1 + 24J_2,$$

$$E_{A15} = -4h + 6J_1 - 24J_2,$$

and  $h_c = 12J_c$ .

As mentioned in Sec. II B,  $F$  and  $A15$  only differ by the occupancy in  $A$  and  $B$  species on the bcc sublattice. If  $2N$  is the total number of sites of this sublattice, we have  $n$  and  $2N - n$  sites occupied by  $A$  and  $B$ , respectively, and the energy of a given configuration, specified by  $n$ , is given by

$$E_n = 2(N - n)\Delta h + E_c,$$

where  $E_c = N(6J_1 - 72J_2)$ .

If  $E_c$  is taken as zero of energy, then the partition function is expressed as

$$Z = \sum_{n=0}^{2N} e^{-2(N-n)\Theta} C_{2N}^n,$$

that is,

$$Z = (2 \cosh \Theta)^{2N}.$$

Let us introduce  $g(\Theta)$ :

$$g(\Theta) = \frac{1}{8N} \ln Z.$$

Then, from the definition of the entropy,

$$\frac{s(\Theta)}{k} = \lim_{T \rightarrow 0} \frac{S(T, \Delta h)}{k} = g(\Theta) - \Theta g'(\Theta),$$

we obtain

$$\frac{s(\Theta)}{k} = \frac{1}{4} \ln(2 \cosh \Theta) - \frac{\Theta}{4} \tanh \Theta$$

and

$$\frac{s'(\Theta)}{k} = -\frac{\Theta}{4 \cosh^2 \Theta}.$$

In order words, no transition exists at finite angle, and the thermodynamical treatment is analytic for  $\Theta$  between 0 and  $\Pi$ . Finally it can be shown that the previous results are given exactly in the Bragg-Williams approximation. Indeed, assuming statistical independency of site occupancies, each site  $n$  is associated with an effective field given by

$$h_n^{\text{eff}} = h - \sum_{m (\neq n)} J_{nm} \langle \sigma_m \rangle$$

and the partition function is simply expressed as

$$Z = \sum_n \varepsilon^{-\beta h_n^{\text{eff}} \sigma_n}.$$

The ensemble average of  $\sigma_n$ , near  $h_c$ , takes the form

$$\langle \sigma_n \rangle = \tanh(\Theta + \beta h_n^{\text{eff}}).$$

Because, when  $T \rightarrow 0$ ,  $h_n^{\text{eff}}$  tends towards zero faster than  $kT$ , we obtain in this limit

$$\langle \sigma_n \rangle \sim \tanh \Theta.$$

Thus, in the Bragg-Williams approximation, the entropy is given by

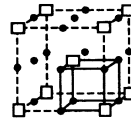
$$\frac{s(\Theta)}{k} = -\frac{1}{4} \left[ \frac{1 + \tanh \Theta}{2} \ln \frac{1 + \tanh \Theta}{2} + \frac{1 - \tanh \Theta}{2} \ln \frac{1 - \tanh \Theta}{2} \right],$$

that is,

$$\frac{s(\Theta)}{k} = \frac{1}{4} \ln(2 \cosh \Theta) - \frac{\Theta}{4} \tanh \Theta.$$

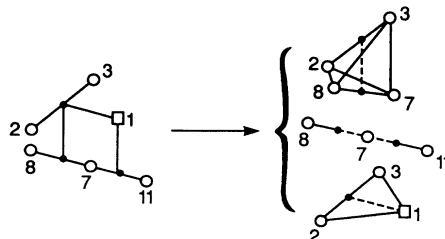
### APPENDIX C

If one replaces each pair belonging to the set of linear chains of the  $A15$  crystalline structure by its center of gravity, then Fig. 1(a) is replaced by Fig. (C1),



(C1)

which represents a simple cubic (sc) lattice with a lattice parameter equal to half the  $A15$  lattice parameter. Then, one can work out the CVM clusters for the  $A15$  structure by analogy with the ones for the sc structure after the reverse transformation is applied. Thus, the first-neighbor pair of sc splits into three different clusters of  $A15$  as illustrated in Fig. (C2) [with site numbers taken from Fig. 1(a)]. The full (empty) circles refer to the sites of the sc ( $A15$ ) lattice; the dash lines indicate a maximum cluster (here a first-neighbor pair) of the sc lattice, which leads, after transformation, to a corresponding cluster of the  $A15$  lattice.



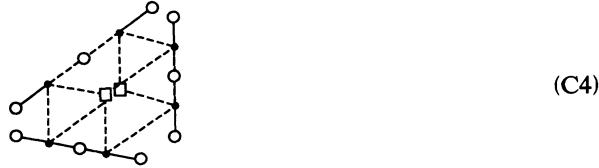
(C2)

For the sc lattice, the next best CVM approximation is achieved by considering the unit square as basic cluster.

By applying the reverse transformation, this cluster leads to the definition of only one six-point cluster for  $A15$  given in Fig. (C3).



The cube cluster of sc is transformed into an 11-point cluster of  $A15$  given in Fig. (C4).



Because the sequence of cluster approximations improves the CVM results with the size of the basic cluster (from pair to square to cube . . .) for the sc lattice, it is intuitively expected that the corresponding sequence defined for  $A15$  will perform similarly.

#### APPENDIX D

We show that near a superdegenerate point, the specific heat  $C$  exhibits a maximum in the low-temperature regime which is not associated to any phase transition but instead to a Schottky anomaly.<sup>24,44</sup>

By definition, at a superdegenerate point, specified by a chemical potential  $h_c$ , there exists an infinity of zero-energy excitations (more precisely, if  $N$  is the number of sites, the number of these excitations increases with  $N$  as  $2^{cN}$ ,  $c > 0$ ). Near  $h_c$ , these excitation energies are very weak and well separated from higher excitation energies. Therefore, when  $T$  increases,  $C$  increases until this first group of excitations is saturated at  $T_s$ . Above this temperature,  $C$  decreases until the next group of states of higher energy is excited. This local maximum, at low temperature, corresponds to a Schottky anomaly, and no phase transition is involved. It is easy to obtain an approximate expression for  $C$ , at low temperature. Let us consider the case of the  $F(A)$ - $A15(A_3B)$  equilibrium, with first- and second-neighbor pair interactions,  $J_1$  and  $J_2$ . To this equilibrium corresponds a superdegenerate point characterized by  $h_c = 12J_2$  ( $h_c = 4.8J_1$  for  $\alpha_2 = 0.4$ ).  $F$  and  $A15$  differ by the occupation of the two simple cubic lattices forming sublattices II. For  $h$  close to  $h_c$ , with  $h > h_c$  (the case  $h < h_c$  can be treated similarly), the lowest-energy excitations are associated with a "spin flip" on a site of sublattice II. The corresponding energy is

given by

$$\Delta E = 2h - 24J_2 = 2\Delta h, \quad \text{where } \Delta h = h - h_c.$$

The next excitations to consider are all multiple of  $\Delta E$ , but their number is more difficult to evaluate. Therefore, we will only retain a subset of these excitations. Let us consider one of the two simple cubic lattices occupied by one type of "spins." The sites of this lattice are connected by an interaction  $J_7$ , not included in our analysis, so that these sites are independent of each other. Thus, any excitation which is associated with a spin flip of  $n$  sites of each individual simple cubic lattice has an energy equal to  $n\Delta E$ . The approximation will consist in considering a two-level system: the ground-state energy (taken as origin of energy) and  $\Delta E$ , the highest energy level being occupied by any number of "particles," between 1 and  $N/8$  ( $N$  is the total number of sites in the  $A15$  lattice). The partition function,  $Z$ , of this system is simply given by

$$Z = (1 + e^{-\beta\Delta E})^{N/8}.$$

The resulting heat capacity per site,  $C$ ,

$$C = \frac{k}{8} (\beta\Delta E)^2 \frac{e^{-\beta\Delta E}}{(1 + e^{-\beta\Delta E})^2},$$

will show a maximum for

$$\frac{\beta\Delta E}{2} = \coth \left[ \frac{\beta\Delta E}{2} \right].$$

With  $\Delta E = 2\Delta h$  and  $\Theta = \beta\Delta h$ , we then have

$$\Theta = \coth\Theta, \quad \text{i.e., } \Theta^* \sim 1.20.$$

Near  $h_c$ , at low temperature,  $C$  will depend on  $T$  and  $h$  only through  $\Theta = \beta\Delta h$ , as expected for any thermodynamical function near a superdegenerate point. The maxima of  $C$  will be found along two lines with slopes given, in a first-order approximation, by  $\Theta^* \sim +1.20$  for  $h > h_c$  and  $\Theta^* \sim -1.20$  for  $h < h_c$ . This behavior has been confirmed with Monte Carlo simulations (cf. Sec. IV B) and the calculated value of  $T_s$  came close to the one deduced from the approximate treatment, i.e.,  $kT_s = \Delta h / \Theta \sim 0.83\Delta h$  (see Fig. 16). Note that these maxima can only be observed at finite  $h$ , i.e., in the grand-canonical ensemble. Indeed, near a superdegenerate point, a study at fixed concentration would lead to an exploration, in the  $(h, T)$  plane, along a line of constant slope  $\Theta$ .

The same treatment would apply to the  $X(A_5B_3)$ - $\bar{X}(A_3B_5)$  equilibrium near  $h_c = 0$ . A similar situation also occurs for an fcc lattice with antiferromagnetic first pair interaction  $J_1$ , near the two superdegenerate points at  $h_c = 4J_1$  and  $12J_1$ .<sup>44</sup>

<sup>1</sup>P. W. Anderson, K. A. Muttalib, and T. V. Ramakrishnan, Phys. Rev. B **28**, 117 (1983).

<sup>2</sup>N. N. Degtyarenko, V. F. Yelesin, and Yu P. Skopintsev, Phys. Met. Metall. (USSR) **62**, 36 (1986).

<sup>3</sup>E. C. van Reuth and R. M. Waterstrat, Acta Crystallogr. Sec.

B **24**, 186 (1968).

<sup>4</sup>R. D. Blaugher, R. E. Hein, J. E. Cox, and R. M. Waterstrat, J. Low Temp. Phys. **1**, 539 (1969).

<sup>5</sup>T. Ishimasa and Y. Fukano, J. Appl. Phys. **22**, 1092 (1983).

<sup>6</sup>D. de Fontaine, in *Solid State Physics*, edited by F. Seitz, D.

- Turnbull, and H. Ehrenreich (Academic, New York, 1979), Vol. 34.
- <sup>7</sup>P. Turchi, M. Sluiter, and D. de Fontaine, *Phys. Rev. B* **36**, 3161 (1987).
- <sup>8</sup>N. C. Tso, M. Kosugi, and J. M. Sanchez, *Acta Metall.* **37**, 121 (1989).
- <sup>9</sup>A. K. Sinha, *Prog. Mater. Sci.* **15**, 79 (1973).
- <sup>10</sup>J. Friedel, *Helv. Phys. Acta* **61**, 538 (1988).
- <sup>11</sup>C. S. Barrett and T. B. Massalski, *Structure of Metals* (Pergamon, Oxford, 1980), Chap. 13.
- <sup>12</sup>L. D. Hartsough, *J. Phys. Chem. Solids* **35**, 1691 (1974).
- <sup>13</sup>E. O. Hall and S. H. Algie, *Metall. Rev.* **11**, 61 (1966).
- <sup>14</sup>D. Schechtman, I. Blech, D. Gratias, and J. W. Cahn, *Phys. Rev. Lett.* **53**, 1951 (1984).
- <sup>15</sup>M. Audier and P. Guyot, in *Extended Icosahedral Structures*, edited by M. V. Jarić and D. Gratias (Academic, New York, 1989), Vol. 3, Chap. 1.
- <sup>16</sup>K. Schubert, *Kristallstrukturen Zweikomponentiger* (Springer, Berlin, 1964).
- <sup>17</sup>W. B. Pearson, *The Crystal Chemistry and Physics of Metals and Alloys* (Wiley, New York, 1972).
- <sup>18</sup>J. Muller, *Rep. Prog. Phys.* **43**, 641 (1980); D. Dew-Hughes, *Cryogenics*, **15**, 435 (1975); L. D. Hartsough, *J. Phys. Chem. Solids* **35**, 1961 (1974); H. D. Wiesinger, *Phys. Status Solidi A* **41**, 465 (1977); Y. Tarutani and M. Kudo, *J. Less Common Met.* **55**, 221 (1977).
- <sup>19</sup>P. Turchi, G. Tréglia, and F. Ducastelle, *J. Phys. F* **13**, 2543 (1983).
- <sup>20</sup>F. Ducastelle and F. Gautier, *J. Phys. F* **6**, 2039 (1976).
- <sup>21</sup>G. Tréglia, B. Legrand, and F. Ducastelle, *Europhys. Lett.* **7**, 575 (1988).
- <sup>22</sup>P. Turchi, Thèse de Doctorat ès Sciences Physiques, University of Paris VI, 1984 (unpublished).
- <sup>23</sup>A. Bieber, F. Ducastelle, G. Tréglia, and P. Turchi, *Solid State Commun.* **45**, 585 (1983); A. Bieber and F. Gautier, *J. Phys. Soc. Jpn.* **53**, 2061 (1984); *Z. Phys. B* **57**, 335 (1984).
- <sup>24</sup>A. Finel, Thèse de Doctorat ès Sciences Physiques, University of Paris VI, 1987 (unpublished), and references therein.
- <sup>25</sup>R. Kikuchi, *Phys. Rev.* **81**, 998 (1951).
- <sup>26</sup>J. M. Sanchez, F. Ducastelle, and D. Gratias, *Physica A* **128**, 334 (1984).
- <sup>27</sup>*Monte Carlo Methods in Statistical Physics*, edited by K. Binder (Springer, Heidelberg, 1979); *Applications of the Monte Carlo Method in Statistical Physics*, edited by K. Binder (Springer, Heidelberg, 1984).
- <sup>28</sup>K. Binder, in *Festkörperprobleme: Advances in Solid State Physics*, edited by P. Grosse (Vieweg, Braunschweig, 1986), Vol. XXVI.
- <sup>29</sup>T. Kudo and S. Katsura, *Prog. Theor. Phys.* **56**, 435 (1976).
- <sup>30</sup>A. Finel and F. Ducastelle, in *Phase Transformations in Solids*, edited by T. Tsakalakos (North-Holland, New York, 1984), p.293.
- <sup>31</sup>A. Finel, D. Gratias, and R. Portier, *L'ordre et le désordre dans les matériaux*, Editions de Physique (Orsay, France, 1984).
- <sup>32</sup>J. L. Lebowitz, M. K. Phani, and D. F. Styer, *J. Stat. Phys.* **38**, 413 (1985).
- <sup>33</sup>T. Morita, *J. Phys. A* **7**, 289 (1974); **7**, 1613 (1974).
- <sup>34</sup>S. A. Pirogov and Ya. G. Sinai, *Teor. Mat. Fiz.* **25**, 358 (1975); **26**, 61 (1976).
- <sup>35</sup>N. D. Mackenzie and A. P. Young, *J. Phys. C* **14**, 3927 (1981); J. Bricmont and J. Slawny, *J. Stat. Phys.* **54**, 89 (1989).
- <sup>36</sup>R. Kikuchi, *J. Chem. Phys.* **66**, 3352 (1977).
- <sup>37</sup>J. A. Barker, *Proc. R. Soc. London, Ser. A* **216**, 45 (1953); J. Hijmans and T. de Boer, *Physica* **21**, 471 (1955); **21**, 485 (1955); **21**, 499 (1955); **22**, 408 (1956); **22**, 429 (1956).
- <sup>38</sup>J. M. Sanchez and D. de Fontaine, *Phys. Rev. B* **17**, 2926 (1978).
- <sup>39</sup>R. Kikuchi (private communication).
- <sup>40</sup>A. Finel, in *Alloy Phase Stability*, Vol. 163 of NATO Advanced Study Institute, Series E, edited by G. M. Stocks and A. Gonis (Kluwer Academic, Dordrecht, 1989), p. 269.
- <sup>41</sup>K. Binder, J. L. Lebowitz, M. K. Phani, and M. H. Kalos, *Acta Metall.* **29**, 1655 (1981).
- <sup>42</sup>R. B. Pandey, D. Stauffer, A. Margolina, and J. G. Zabolitzky, *J. Stat. Phys.* **34**, 427 (1984).
- <sup>43</sup>T. Mohri, J. M. Sanchez, and D. de Fontaine, *Acta Metall.* **33**, 1463 (1985).
- <sup>44</sup>A. Finel and F. Ducastelle, *Europhys. Lett.* **1**, 135 (1986); R. Tétot, A. Finel, and F. Ducastelle, *J. Stat. Phys.* **61**, 121 (1990).
- <sup>45</sup>R. Haydock, V. Heine, and M. Kelly, *J. Phys. C* **5**, 2845 (1972); R. Haydock, in *Solid State Physics*, edited by F. Seitz, D. Turnbull, and H. Ehrenreich (Academic, New York, 1980), Vol. 35, p. 216.
- <sup>46</sup>N. Saunders and A. P. Miodownik, *J. Mater. Sci.* **22**, 629 (1987).
- <sup>47</sup>Ya P. Yarmolyuk and P. I. Kripyakevich, *Kristallografiya* **19**, 539 (1974) [*Sov. Phys. Crystallogr.* **19**, 334 (1974)]; K. H. Kuo, Y. Q. Ye, and D. X. Li, *J. Mater. Sci.* **21**, 2597 (1986); D. P. Shoemaker and C. B. Shoemaker, *Act. Crystallogr. Sec. B* **42**, 3 (1986).
- <sup>48</sup>S. Andersson, *J. Solid State Chem.* **23**, 191 (1978).
- <sup>49</sup>L. A. Bursill and B. G. Hyde, *Nature Phys. Sci.* **240**, 122 (1972); M. Arita, H.-U. Nissen, and W. Schauer, *Philos. Mag. Lett.* **60**, 161 (1989).

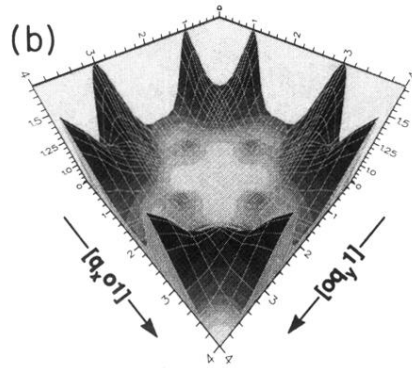
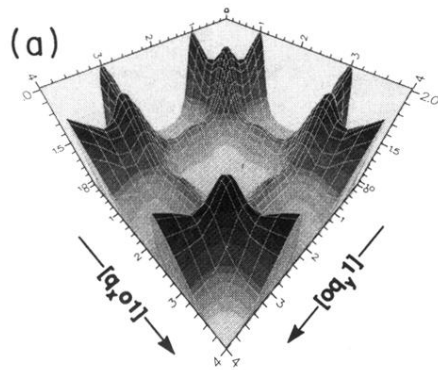


FIG. 22. SRO diffuse scattering intensity in the (001) plane with  $q_z=1.0$  as computed with the PSC-CVM-BW.  $\alpha_2=0.4$ ,  $\alpha_7=-0.01$ ,  $kT/J_1=2.0$ , and  $h/J_1=1.0$  (a),  $h/J_1=3.5$  (b).

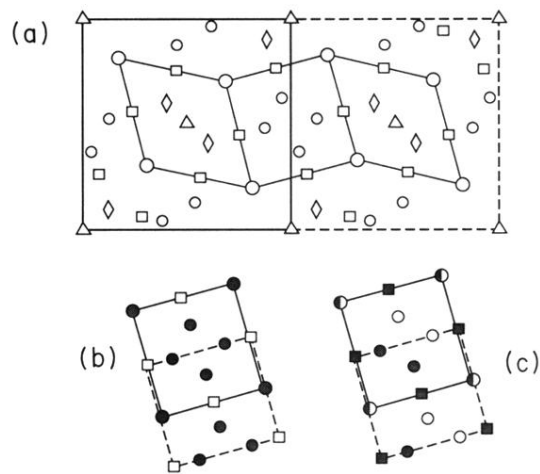


FIG. 25. (a) Projection along the  $c$  axis of two unit cells of the  $\sigma$  phase:  $\Delta$ ,  $\diamond$ ,  $\circ$ ,  $\square$ ,  $\circ$  refer to sites of sublattices  $A$ ,  $B$ ,  $C$ ,  $D$ , and  $E$ , respectively. The rhombi and the square delimited by thin lines indicate the two kinds of building blocks ( $Z$  and  $A_{15}$ , respectively) constituting the  $\sigma$  phase. (b) and (c) specify the chemical order on various sites of the  $\sigma$  phase constrained by a local configuration of the  $A_{15}$  ( $A_3B$ ) or  $X$  ( $A_5B_3$ ) type, respectively. Full or empty sites in (b) and (c) refer to  $A$  or  $B$  species, respectively.

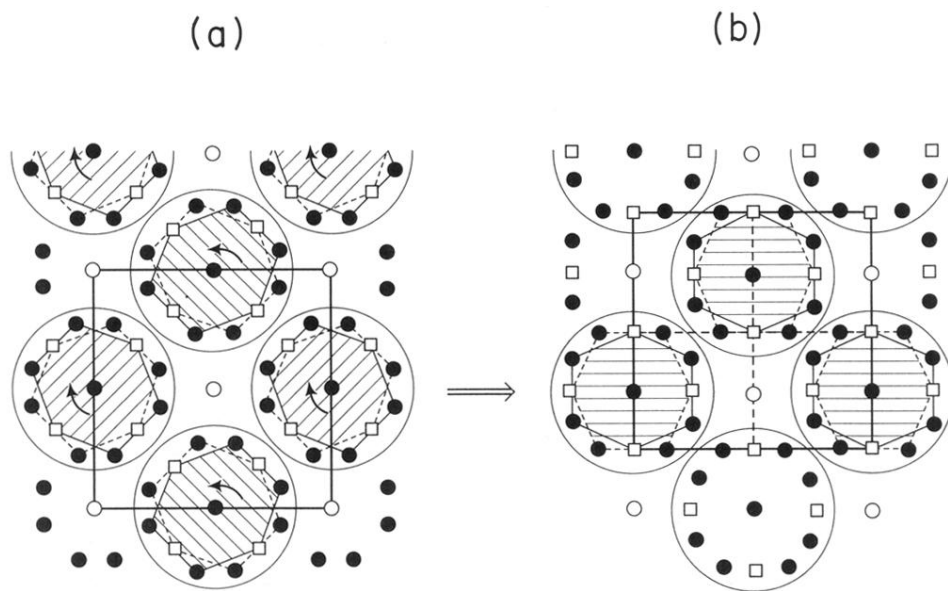


FIG. 26. (a) Projection along the  $c$  axis of the  $D8_m$  crystalline structure (of  $W_5Si_3$  type). One unit cell is specified within the thick solid line. The full and empty circles and empty squares refer to the three inequivalent sites of the structure occupied by  $A$  (full symbols) and  $B$  (empty symbols) species (final composition:  $A_5B_3$ ). By applying a Hyde rotation, i.e., a collective rotation of the sites inscribed in each cylinder, of  $\pi/4$  in a direction indicated by the arrow, the transformed structure represented in (b) is described by four  $A15$  unit cells.